



**HAL**  
open science

## The representation of sea salt aerosols and their role in polar climate within CMIP6

Rémy Lapere, Jennie L Thomas, Louis Marelle, Annica M. L. Ekman, Markus M Frey, Marianne Tronstad Lund, Risto Makkonen, Ananth Ranjithkumar, Matthew E Salter, Bjørn Hallvard Samset, et al.

### ► To cite this version:

Rémy Lapere, Jennie L Thomas, Louis Marelle, Annica M. L. Ekman, Markus M Frey, et al.. The representation of sea salt aerosols and their role in polar climate within CMIP6. *Journal of Geophysical Research: Atmospheres*, In press, pp.e2022JD038235. 10.1029/2022jd038235 . insu-04020054v1

**HAL Id: insu-04020054**

**<https://insu.hal.science/insu-04020054v1>**

Submitted on 8 Mar 2023 (v1), last revised 16 Mar 2023 (v2)

**HAL** is a multi-disciplinary open access archive for the deposit and dissemination of scientific research documents, whether they are published or not. The documents may come from teaching and research institutions in France or abroad, or from public or private research centers.

L'archive ouverte pluridisciplinaire **HAL**, est destinée au dépôt et à la diffusion de documents scientifiques de niveau recherche, publiés ou non, émanant des établissements d'enseignement et de recherche français ou étrangers, des laboratoires publics ou privés.

# The representation of sea salt aerosols and their role in polar climate within CMIP6

Rémy Lapere<sup>1</sup>, Jennie L. Thomas<sup>1</sup>, Louis Marelle<sup>2</sup>, Annica M. L. Ekman<sup>3,4</sup>, Markus M. Frey<sup>5</sup>, Marianne Tronstad Lund<sup>6</sup>, Risto Makkonen<sup>7</sup>, Ananth Ranjithkumar<sup>5</sup>, Matthew E. Salter<sup>3,8</sup>, Bjørn Hallvard Samset<sup>6</sup>, Michael Schulz<sup>9</sup>, Larisa Sogacheva<sup>7</sup>, Xin Yang<sup>5</sup>, Paul Zieger<sup>3,8</sup>

<sup>1</sup>Univ. Grenoble Alpes, CNRS, IRD, Grenoble INP\*, IGE, 38000 Grenoble, France

<sup>2</sup>LATMOS/IPSL, Sorbonne Université, UVSQ, CNRS, Paris, France

<sup>3</sup>Department of Meteorology, Stockholm University, Stockholm, Sweden

<sup>4</sup>Bolin Center for Climate Research, Stockholm, Sweden

<sup>5</sup>Natural Environment Research Council, British Antarctic Survey, Cambridge, UK

<sup>6</sup>CICERO Center for International Climate Research, Oslo, Norway

<sup>7</sup>Finnish Meteorological Institute, Climate Research Programme, Helsinki, Finland

<sup>8</sup>Department of Environmental Science, Stockholm University, Stockholm, Sweden

<sup>9</sup>Norwegian Meteorological Institute, Oslo, Norway

\*Institute of Engineering and Management Univ. Grenoble Alpes

## Key Points:

- CMIP6 models have a large uncertainty in present day sea salt aerosol abundance at the poles
- Model performance is degraded closer to the poles suggesting inadequate emission sources within the polar regions
- Both present and future radiative balance at the poles is uncertain because of sea salt aerosols

---

Corresponding author: Rémy Lapere, [remy.lapere@univ-grenoble-alpes.fr](mailto:remy.lapere@univ-grenoble-alpes.fr)

Corresponding author: Jennie L. Thomas, [jennie.thomas@univ-grenoble-alpes.fr](mailto:jennie.thomas@univ-grenoble-alpes.fr)

This article has been accepted for publication and undergone full peer review but has not been through the copyediting, typesetting, pagination and proofreading process, which may lead to differences between this version and the [Version of Record](#). Please cite this article as [doi: 10.1029/2022JD038235](https://doi.org/10.1029/2022JD038235).

This article is protected by copyright. All rights reserved.

Accepted Article

## Abstract

Natural aerosols and their interactions with clouds remain an important uncertainty within climate models, especially at the poles. Here, we study the behavior of sea salt aerosols (SSaer) in the Arctic and Antarctic within 12 climate models from CMIP6. We investigate the driving factors that control SSaer abundances and show large differences based on the choice of the source function, and the representation of aerosol processes in the atmosphere. Close to the poles, the CMIP6 models do not match observed seasonal cycles of surface concentrations, likely due to the absence of wintertime SSaer sources such as blowing snow. Further away from the poles, simulated concentrations have the correct seasonality, but have a positive mean bias of up to one order of magnitude. SSaer optical depth is derived from the MODIS data and compared to modeled values, revealing good agreement, except for winter months. Better agreement for AOD than surface concentration may indicate a need for improving the vertical distribution, the size distribution and/or hygroscopicity of modeled polar SSaer. Source functions used in CMIP6 emit very different numbers of small SSaer, potentially exacerbating cloud-aerosol interaction uncertainties in these remote regions. For future climate scenarios SSP126 and SSP585, we show that SSaer concentrations increase at both poles at the end of the 21<sup>st</sup> century, with more than two times mid-20<sup>th</sup> century values in the Arctic. The pre-industrial climate CMIP6 experiments suggest there is a large uncertainty in the polar radiative budget due to SSaer.

## Plain Language Summary

Aerosols emitted from the ocean, such as sea salt particles (aerosols), are critical for the climate of polar regions. However, there is still uncertainty in their representation in climate models. The purpose of this work is to evaluate the representation of sea salt aerosols in the Arctic and Antarctic in a recent model inter-comparison initiative, and to assess the consequences for our understanding of present-day and future polar climate. We find that the models disagree between them and with observations from ground stations and from space. This suggests that the formulation of sea salt emissions in global models is not adapted for polar regions. With sea ice retreat, sea salt aerosols will most likely increase in the future, which makes addressing the current uncertainty an important next step for the scientific community.

## 1 Introduction

The polar regions have a larger sensitivity to changes in global climate than any other region (Manabe & Wetherald, 1975; Meredith et al., 2019). This is called polar amplification, which refers to the multiple factors that control why polar regions are changing faster than the rest of the planet. A key reason for polar amplification is sea ice and snow loss, which changes surface albedo from light to dark and induces an additional regional warming, or climate feedback (Hall, 2004). Atmospheric temperature feedbacks such as the Planck feedback and local lapse-rate feedback also play an important role in this amplification (Stuecker et al., 2018). Rantanen et al. (2022) found that climate models and observational data disagree on the magnitude of Arctic amplification over the past 40 years, with larger trends found in observations. Climate models capture some aspects of polar amplification, but not all of the complexity of what is occurring within the rapidly changing polar regions, in particular in the Antarctic where the model bias is even more pronounced (D. M. Smith et al., 2019).

Clouds are a key, uncertain component of the polar and global climate system (Flato et al., 2013). Specifically, clouds can have both a cooling (via reflection of shortwave radiation) and warming (by trapping longwave radiation) effect on the polar atmosphere, depending on their optical thickness and cloud droplet number as reviewed in Alkama et al. (2020). As a result, polar clouds in summer have the potential to dampen the ra-

74 diative impact of sea ice loss through shortwave cooling (Alkama et al., 2020), but sum-  
75 mertime low-level clouds in the Arctic can also favor sea ice melt through longwave warm-  
76 ing (Y. Huang et al., 2021). In wintertime, the surface cloud forcing at the poles is stronger  
77 than in summer and with a warming effect (Curry et al., 1996).

78 Aerosols are also a key uncertainty in climate models globally and have even larger  
79 uncertainties in the polar regions (Sand et al., 2017). Aerosols influence the climate through  
80 their interaction with radiation directly (aerosol direct effect) and their role in cloud for-  
81 mation/modification (aerosol indirect and semi-direct effects) (Myhre et al., 2013). Nat-  
82 ural sources of aerosols and their impacts on clouds have been less of a focus than un-  
83 derstanding anthropogenic aerosols and their direct and indirect radiative effects (Schmale  
84 et al., 2021; Boucher et al., 2013; Sand et al., 2021; Samsset, 2022). However, it is chal-  
85 lenging to separate the effects on clouds and radiation of anthropogenic and natural aerosols,  
86 and these effects can have opposite signs, including at the poles (Allen & Sherwood, 2011).  
87 In addition, cloud-aerosol interactions are non-linear (Gryspeerd et al., 2019), so esti-  
88 mating anthropogenic impacts on polar clouds requires an accurate understanding of the  
89 natural aerosol baseline. Therefore improved representation of natural aerosols and their  
90 impacts on clouds are essential for improved anthropogenic climate change estimates.

91 Sea salt particles resulting from sea spray make up most of the aerosol mass over  
92 oceanic regions (Andreae & Rosenfeld, 2008), with an even larger fraction over the po-  
93 lar regions (Sand et al., 2017). Sea spray is composed of a mixture of inorganic salts and  
94 an organic fraction (including both dissolved organics and fragments of organic mate-  
95 rial). In this study, we focus on the inorganic fraction of sea spray emissions and use the  
96 wording sea salt aerosols (SSaer) to refer to the inorganic fraction (sodium chloride, sul-  
97 fate, and other trace salt species) of sea spray. When discussing sea spray we refer to the  
98 full mixture of emitted species, which includes both inorganic and organic marine aerosols.

99 SSaer and sulfate emitted from sea spray can act as Cloud Condensation Nuclei  
100 (CCN) (Prank et al., 2022; Xu et al., 2022), and marine organics can act as Ice Nucle-  
101 ating Particles (INP) (Wilson et al., 2015; DeMott et al., 2016). Over polar oceans, sea  
102 spray aerosols including SSaer can seasonally make up most of the cloud seeding pop-  
103 ulation (Quinn et al., 2017; Fossum et al., 2018). They also scatter incoming solar short-  
104 wave radiation directly (Takemura et al., 2002; Satheesh & Lubin, 2003). In addition,  
105 SSaer also change the climate impacts of other species, including anthropogenic pollu-  
106 tants such as nitrate (Chen et al., 2020) and sulfate (Fossum et al., 2020), by regulat-  
107 ing their droplet activation. Furthermore, SSaer modulate polar atmospheric chemistry  
108 by providing a surface for heterogeneous reactions and leading to bromine activation, with  
109 major effects on ozone and mercury depletion events (Hara et al., 2018; Zhu et al., 2019;  
110 Marelle et al., 2021). Accurately modeling sea spray aerosols, including inorganic SSaer,  
111 is therefore a prerequisite for properly representing the polar atmosphere. In particu-  
112 lar, the SSaer physical parameters key to their cloud and radiation interaction and re-  
113 moval processes, are the number flux, the size distribution, and the hygroscopicity.

114 Sea spray emission over the open ocean is due to wind action that forms bursting  
115 bubbles at the sea surface, visible as white caps, which emit aerosols to the atmosphere  
116 (Monahan et al., 1986). The sea surface temperature (SST) can also modulate the size  
117 and number of aerosols emitted (Mårtensson et al., 2003; Jaeglé et al., 2011; Salter et  
118 al., 2015; Liu et al., 2021). Salinity affects the electrolytic properties of water, and as salin-  
119 ity increases, coalescence is inhibited and bubbles form in larger number and smaller radii,  
120 which then also affects the emission flux of SSaer (Zinke et al., 2022). There remain sig-  
121 nificant uncertainties in the open ocean sourced sea spray aerosol emission fluxes, includ-  
122 ing the relatively well-studied inorganic SSaer, that is emitted into the atmosphere, es-  
123 pecially at the cold temperatures in the polar regions. For example, Regayre et al. (2020)  
124 found that sea spray emissions in the Southern Ocean needed to be tripled in a global  
125 simulation to match observations. Unlike other oceanic areas in the world that remain  
126 open throughout the year, estimates of sea spray emissions at the poles depend on a proper

127 representation of sea ice cover, which is still challenging in climate models and exhibits  
128 a large spread in model ensembles (Notz & SIMIP Community, 2020; Roach et al., 2020).  
129 Additional polar-specific source processes of SSAer include blowing snow over sea ice (Yang  
130 et al., 2008; J. Huang & Jaeglé, 2017; Yang et al., 2019; Marelle et al., 2021) and emis-  
131 sion fluxes specific to open water leads (Held et al., 2011; Kirpes et al., 2019; Ioannidis  
132 et al., 2022). Climate models parameterize emissions from open water leads in sea ice  
133 like those from the open ocean, even though wave action and white caps are very dif-  
134 ferent in leads than in open ocean due to e.g., reduced wind fetch, local convection, and  
135 the lack of a surf zone on the sea-ice edge (Nilsson et al., 2001). Blowing snow sources  
136 of SSAer on the other hand are usually not included in global models and to our knowl-  
137 edge are not included in CMIP6 models.

138 Due to the ongoing trend of sea ice retreat (Meredith et al., 2019), sea spray emis-  
139 sions at the poles are likely to increase in the coming decades. Specifically, less sea ice  
140 means more open ocean and therefore more sea spray (Struthers et al., 2013). In par-  
141 allel, increased sea spray emissions probably have a negative effective radiative forcing  
142 globally (Thornhill et al., 2021), including at the poles (Korhonen et al., 2010; Browse  
143 et al., 2014), where it is likely dominated by the aerosol-cloud interaction (Struthers et  
144 al., 2011). The cooling induced by SSAer-cloud interactions could partially compensate  
145 for the warming caused by sea ice loss. Accurate representation of SSAer in the atmo-  
146 sphere is also important for reliable future climate projections. However, both AeroCom  
147 (Sand et al., 2017) and the Coupled Model Intercomparison Project phase 6 (CMIP6)  
148 (Mortier et al., 2020; Gliß et al., 2021) reported a large uncertainty in the aerosol bud-  
149 get and seasonality, globally and at the poles. Fanourgakis et al. (2019) also indicated  
150 significant model diversity of up to two orders of magnitude in simulated SSAer concen-  
151 trations over the Southern Ocean, resulting from different parameterizations in global  
152 models.

153 In the present work, we address the following science questions:

- 154 1. How diverse are SSAer emissions/concentrations at the poles in CMIP6 models?
- 155 2. What are the drivers of this model diversity?
- 156 3. How well do the CMIP6 models and ensembles represent SSAer at the poles rel-  
157 ative to surface observations and remote sensing?
- 158 4. What are the implications of model diversity and changes in SSAer emissions, for  
159 the present and future polar climate?

160 To answer these questions, we conduct an assessment of polar SSAer diversity in CMIP6  
161 models in Section 3.1, by comparing SSAer related variables in the CMIP6 historical ex-  
162 periment. We further evaluate the models against SSAer concentration data from mea-  
163 surement stations and aerosol optical depth from the Moderate-Resolution Imaging Spec-  
164 troradiometer (MODIS) Aqua and Terra satellite products in Section 3.2. Finally, in Sec-  
165 tion 3.3 we analyze the historical and future trends of SSAer in the Shared Socioeconomic  
166 Pathways 126 and 585 scenarios and the sensitivity of the polar radiative budget to changes  
167 in SSAer emissions, through different CMIP6 experiments to shed light on the implica-  
168 tions of modeling discrepancies in CMIP6.

## 169 2 Materials and Methods

### 170 2.1 Models

171 We use results from 12 climate models that are part of CMIP6. Models were sel-  
172 ected based the availability of relevant variables for the evaluation of SSAer. The mod-  
173 els included, along with the available variables and source function formulation are in-  
174 dicated in Table 1. Only one additional CMIP6 model features the mass mixing ratio  
175 of sea salt aerosol variable ( $mmr_{ss}$ ) for the historical experiment (INM-CM5). We have

176 chosen to discard this model because it produces unrealistic SSAer concentrations that  
177 are three orders of magnitude larger than any other model. All other CMIP6 models are  
178 excluded because they do not provide *mmr<sub>ss</sub>* in the historical experiment.

179 In order to evaluate the representation polar SSAer within CMIP6 models, we ex-  
180 tracted the following from the Earth System Grid Federation (ESGF) platform (ESGF,  
181 2014), for the historical CMIP6 experiment (run with coupled ocean-atmosphere mod-  
182 els) and for the period 1951–2014 (as summarized in Table 1): mass mixing ratio of sea  
183 salt aerosol (*mmr<sub>ss</sub>*), sea salt aerosol emission flux (*emiss*), sea ice concentration (*siconc*),  
184 surface wind speed (*sfcWind*), optical depth of sea salt aerosol at 550 nm (*od550ss*) and  
185 planetary boundary layer height (*bldep*). We use this information for all 12 models, but  
186 exclude variables that were missing as output on the ESGF platform for certain mod-  
187 els.

188 Future projections are also considered in this work, relying on the Shared Socio-  
189 economic Pathway (SSP) 126 and 585 experiments (ScenarioMIP activity - O’Neill et al.  
190 (2016)). Here, we consider the two extreme scenarios, SSP126 and SSP585. SSP126 rep-  
191 represents the low end of the range of plausible future pathways, where radiative forcing reaches  
192 a level of approximately  $2.6 \text{ W m}^{-2}$  in 2100 compared to the pre-industrial period. SSP585  
193 is at the other end of the spectrum, with a radiative forcing of approximately  $8.5 \text{ W m}^{-2}$   
194 at the end of the century. In both of these scenarios, the Arctic surface air temperature  
195 warms more than the global mean. The change in temperature between 2000–2014 and  
196 2085–2100 is different by a factor of around 2 between the global and Arctic average ( $3.8^\circ\text{C}$   
197 versus  $1.5^\circ\text{C}$  in SSP126 and  $10.8^\circ\text{C}$  versus  $5.1^\circ\text{C}$  in SSP585, respectively), and with a  
198 large uncertainty (model spread - in the sense of the difference between minimum and  
199 maximum increase - of  $7^\circ\text{C}$  in SSP126 and  $10^\circ\text{C}$  in SSP585). In contrast, the Antarc-  
200 tic has a lower warming than the global mean in both scenarios (Table A1). Other SSP  
201 scenarios are provided in CMIP6, including intermediate trajectories in between SSP126  
202 and SSP585. However, we chose to select only the two extreme SSPs for this work in or-  
203 der to obtain lower and upper boundaries of the changes of polar SSAer.

204 The significance, sign and magnitude of trends in these scenarios are calculated us-  
205 ing a Mann-Kendall test (Mann, 1945). For the evaluation of SSAer radiative impact,  
206 two experiments of the AerChemMIP activity are considered. For that, the top-of-atmosphere  
207 net downward radiation flux (*rtmt*) and near-surface air temperature (*tas*) in experiments  
208 *piClim-2xss* and *piClim-control* pre-industrial (30 years under 1850 climate) atmospheric  
209 composition scenarios are investigated.

210 For spatial ensemble means, model output is first re-gridded to a common grid, to  
211 the lowest model resolution available ( $3^\circ\text{lon} \times 2^\circ\text{lat}$ ). The re-gridding is done using Cli-  
212 mate Data Operators bilinear remapping tool (Schulzweida et al., 2012). For regionally  
213 averaged numbers, a weighted mean is applied, with weights corresponding to the grid  
214 cell area. Ground station data usually provide a mass concentration of sodium, whereas  
215 models output the SSAer mass mixing ratio. For the comparison between the two, the  
216 SSAer mass mixing ratio is therefore converted into a mass concentration under a stan-  
217 dard air density at 1 atmosphere and  $0^\circ\text{C}$  temperature ( $1.2922 \text{ kg m}^{-3}$ ). SSAer in the mod-  
218 els is assumed to follow the composition of Seinfeld and Pandis (2016), and sodium mass  
219 is thus taken as 30.61% of SSAer mass. Near-surface concentration in the models refers  
220 to the concentration within the lowest vertical level. Furthermore, the atmospheric life-  
221 time of SSAer is calculated as the global load (that is, the integral of *mmr<sub>ss</sub>* on the ver-  
222 tical levels for each latitude and longitude) divided by the global emission rate, weighted  
223 by grid cell area. We do not use deposition for the the lifetime analysis because it is only  
224 available for 8 out of the 12 models. A comparison (not shown here) of the results us-  
225 ing total deposition (dry+wet) instead of emissions where possible for this computation  
226 shows minor differences that do not affect the conclusions for most models. However, two  
227 models (CESM and MPI-ESM) simulate different budgets for emission and deposition,  
228 leading to different computed lifetimes (up to 30%). This might suggest too much SSAer

229 accumulation in the atmosphere in these two models. Discrepancies in the emission or  
230 deposition diagnostics used in the models could also explain this difference. This is not  
231 investigated in this work. The metrics used to compare models and observations are the  
232 normalized mean bias (NMB), defined as  $NMB = (\langle MODEL \rangle - \langle OBS \rangle) / \langle OBS \rangle$ ,  
233 where  $\langle . \rangle$  is the annual mean, and the Pearson correlation coefficient, simply referred  
234 to as correlation (R).

235 Among the 12 models considered, sea spray emissions are parameterized by 8 dif-  
236 ferent source functions or combinations of source functions (Table 1). The common fea-  
237 ture of these source functions is that for a given aerosol radius, the emission flux is pro-  
238 portional to the wind speed raised to a varying exponent. Some of the parameterizations  
239 also account for the dependence of sea spray emissions on SST. Although there is still  
240 debate on the exact role that SST plays in the sea spray emission process, including it  
241 generally improves the fit with observations as reviewed in Grythe et al. (2014). For ex-  
242 ample, the Jaeglé et al. (2011) parameterization decreases emissions at colder SST, whereas  
243 the Salter et al. (2015) source function does the opposite. For polar waters, for exam-  
244 ple, an increase in SST may decrease the number of sea spray aerosol produced, with-  
245 out significantly affecting the shape of the size distribution (Zábori et al., 2012). This  
246 is consistent with the Salter et al. (2015) source function, but opposite to the SST de-  
247 pendence in the Jaeglé et al. (2011) source function, for which emissions increase at higher  
248 SST. This shows that not all source functions may be fit for use in polar regions. The  
249 source functions are further investigated in Section 3.1.2 based on offline calculations from  
250 the source function formulations, using a sectional approach with fixed bins, regardless  
251 of what is actually done in the models. This approach is used to evidence the diversity  
252 coming from the source functions themselves rather than the aerosol schemes of the mod-  
253 els.

254 To our knowledge, polar-specific sources of SSAer such as blowing snow over sea ice  
255 and emissions from leads are not taken into account in CMIP6 climate models, which  
256 may limit their performance at high latitudes. Measurement campaigns have shown that  
257 such sea ice related sources can be an important contributor to SSAer load in winter (Kirpes  
258 et al., 2019; Frey et al., 2020). Similarly, only the fraction of the ocean that is ice-free  
259 can lead to sea spray emissions. Therefore, SSAer emissions at the poles in climate mod-  
260 els are highly dependent on a proper representation of sea ice cover. As a consequence,  
261 SSAer emissions are probably harder to adequately model at the poles than in any other  
262 oceanic region in the world. However, even for mid-latitudes and more generally glob-  
263 ally, climate models disagree on SSAer representation, such as their total emission fluxes,  
264 lifetime, burden, and optical properties including hygroscopicity (Burgos et al., 2020; Glib  
265 et al., 2021). The sinks of SSAer such as dry and wet deposition, control their atmospheric  
266 quantities. Accurate wet deposition rates require adequate precipitation, which is chal-  
267 lenging for Antarctica (Roussel et al., 2020) and the Arctic (Diaconescu et al., 2018) in  
268 climate models. In parallel, dry deposition of aerosols is sensitive to the choice of depo-  
269 sition velocity, which is usually not tuned for snow-covered terrain in chemistry-transport  
270 models, resulting in large uncertainties in the Arctic (Qi et al., 2017). Dry deposition  
271 is also sensitive to boundary layer stability, which is difficult to model especially in po-  
272 lar regions (Holtslag et al., 2013). Finally, the transport of aerosols from the mid-latitudes  
273 to the poles can also represent a source of uncertainty in the models. Therefore, it is not  
274 expected that climate models would converge in regions as complex as the poles, where  
275 in addition to emission fluxes, meteorology (Cai et al., 2021) and anthropogenic aerosol  
276 budgets (Sand et al., 2017) are more challenging to represent.

### 277 *2.1.1 Reanalysis*

278 In order to assess how CMIP6 models compare with more widely used air quality-  
279 oriented reanalyses, this work includes two monthly reanalysis products. The Modern-  
280 Era Retrospective analysis for Research and Applications, Version 2 (Global Modeling

281 and Assimilation Office, 2015, MERRA2) and the Copernicus Atmosphere Monitoring  
282 Service (Inness et al., 2019, CAMS). For the former, the Sea Salt Surface Mass Concen-  
283 tration (*SSMASS*) variable from the *tavg1\_2d\_aer\_Nx* monthly product is considered,  
284 over the period 1980–2021. For the latter, the *CAMS global reanalysis (EAC4) monthly*  
285 *averaged fields* product is used and the three size bins of the *Sea salt aerosol mixing ra-*  
286 *tio* variable are summed and taken at the first model level, over the period 2003–2021.  
287 We also use the monthly climatology of sea ice concentration from the fifth generation  
288 ECMWF atmospheric reanalysis of the global climate (Hersbach et al., 2019, ERA5).

## 289 2.2 Observations

### 290 2.2.1 Ground based stations

291 Combining data from the literature (Legrand et al., 2016; Yang et al., 2019) and  
292 from the EBAS platform (Norwegian Institute for Air Research, 2022), sodium aerosol  
293 concentration measurements were obtained over a multiyear period for 9 stations in the  
294 Arctic and 5 in the Antarctic. Their location, the data source, and the period covered  
295 by the observations are detailed in Figure 1. When taken from the EBAS platform, the  
296 weekly measurements of atmospheric sodium, typically conducted using high-volume air  
297 samplers, are then averaged to obtain the annual cycle of monthly means and the related  
298 standard deviations, over the entire time period in the data set. We use these observa-  
299 tions without assuming a particular cut-off size and directly compare to the total sodium  
300 mass derived from the modeled SSaer (maximum radii in the models can be found in Ta-  
301 ble 1).

302 The nine Arctic stations include two sites above 80°N (Alert and Villum) in Canada  
303 and Greenland, respectively. These two coastal sites are surrounded by sea ice even in  
304 summer (blue contour in Figure 1). Data from a third coastal site (Utqiagvik, Alaska,  
305 71°N) is available, where, in contrast to Alert and Villum, the shore is sea ice free in sum-  
306 mer but sea ice covered in winter. Summit (Greenland) is an inland station in the mid-  
307 dle of Greenland. Zeppelin (Svalbard) is a mountainous site (475 m a.s.l.) near the shore  
308 of a fjord at 79°N, which is more and more influenced by sea spray (Heslin-Rees et al.,  
309 2020). The rest of the Arctic stations considered in this work are in northern Europe (Irafoss  
310 in Iceland, Pallas in Finland, Karasjok in Norway and Bredkälén in Sweden). For Antarc-  
311 tica, one of the five stations is far inland (Concordia), one is on the coast of East Antarc-  
312 tica (Dumont d’Urville) and the three others are in coastal western Antarctica (Halley,  
313 Neumayer, Palmer). These stations are located between 65°S and 75°S (Figure 1). The  
314 sodium aerosol concentration measurement data provided for these stations do not in-  
315 clude information on measurement uncertainty. Theoretically, high volume samplers carry  
316 a  $\pm 0.04 \mu\text{g m}^{-3}$  precision for particulate matter mass collected on filters, although this  
317 uncertainty is highly dependent on environmental factors (McCurry, 2000).

### 318 2.2.2 Satellite remote sensing

319 A regional evaluation of SSaer in CMIP6 is conducted by comparing its modeled  
320 optical depth with aerosol optical depth (AOD) satellite data from MODIS (Platnick,  
321 2015). To our knowledge, there is no pure satellite climatology for SSaer AOD. Those  
322 products available such as MACv2 (Kinne, 2019) usually include a modeled component  
323 in their climatology. For the purpose of this CMIP6 model evaluation, a proxy based on  
324 MODIS AOD and Angstrom exponent is therefore used to create a simple version of this  
325 missing product. A more refined dedicated polar marine AOD climatology product could  
326 be created by combining several satellite sources (Dror et al., 2018; Dasarathy et al., 2021;  
327 Atmoko & Lin, 2022) in future work. However, the Arctic time series obtained using the  
328 methodology described below (Section 3.2.2) is well in line with the SSaer AOD values  
329 reported in Xian et al. (2022) for example, which are based on an ensemble of reanal-  
330 yses. This suggests that the simple proxy used here yields reasonable values of SSaer AOD.



331 This custom product is based on the MODIS Atmosphere L3 Monthly Products  
332 MOD08\_M3 (from satellite Terra) and MYD08\_M3 (from satellite Aqua) (Platnick, 2015)  
333 for the period 2005–2014. The monthly mean AOD at 550 nm is taken from the Dark  
334 Target/Deep Blue (DTDB) combined variable *AOD\_550\_Dark\_Target\_Deep\_Blue\_Combined\_Mean\_Mean*.  
335 This AOD product carries an uncertainty of around 0.03 (Sayer et al., 2013). Then, a  
336 filter is applied that aims at keeping only the contribution of SSAer to AOD. This filter  
337 is based on the condition that the Angstrom exponent is below 1 to filter out fine-mode  
338 aerosols. The implied assumptions are that SSAer are dominated by coarse-mode par-  
339 ticles and that coarse-mode aerosols over the polar oceans are dominated by SSAer. The  
340 former is shown in e.g. Murphy et al. (2019), the latter assumption is discussed in the  
341 next paragraph. The *Aerosol\_AE1\_Ocean\_JHisto\_vs\_Opt\_Depth* variable from MOD08\_M3  
342 and MYD08\_M3 is used to discriminate Angstrom exponents. It contains, for each month  
343 and grid cell, a joint histogram of the calculated Angstrom exponent (0.55–0.86  $\mu\text{m}$ ) ver-  
344 sus retrieved AOD at 550 nm. This variable provides data only over oceans, and as a re-  
345 sult the product we build here is only valid for oceans. We use it as follows: for each grid  
346 cell and month, the frequency of records with  $\text{AE} < 1$  i.e.  $\text{Freq}_{\text{AE} < 1} = \text{Counts}_{\text{AE} < 1} / \text{Counts}_{\text{AE}}$   
347 is computed, regardless of the AOD joint distribution. The DTDB 550 nm AOD is then  
348 multiplied by this  $\text{Freq}_{\text{AE} < 1}$  factor to approximate the fraction of AOD attributable to  
349 coarse-mode aerosols, and by extension SSAer. The resulting estimated fraction of AOD  
350 from MODIS attributed to SSAer is referred to as AOD<sub>ss</sub> in the continuation. The al-  
351 gorithm created to build this AOD<sub>ss</sub> extraction from MODIS is attached to this paper.

352 The key assumption for the validity of this approach is that coarse-mode aerosols  
353 in the MODIS records are dominated by SSAer over polar oceans and therefore that dust  
354 has a minor contribution. This hypothesis is supported by the MACv2 aerosol clima-  
355 tology (Kinne, 2019), which provides AOD based on AERONET/MAN and climate mod-  
356 els, with species differentiation. We use this data set to evaluate the contribution of SSAer  
357 AOD to {SSAer+dust} AOD and assess the validity of the assumption that dust is not  
358 an important fraction. In this data set, the fraction of {SSAer+dust} AOD attributed  
359 to SSAer is well above 80% over most of the polar oceans, except in coastal areas where  
360 important dust sources can be found (Meinander et al., 2022) and the central Arctic, which  
361 is permanently covered with sea ice (Figure 1). For these regions, however, AOD in MACv2  
362 is very low and/or dominated by the fine-mode fraction, which is filtered out by our Angstrom  
363 exponent criterion. Therefore the MACv2 product supports the assumption that coarse-  
364 mode AOD over the polar oceans is essentially SSAer AOD, as illustrated in Figure A1.  
365 Sporadic transport events of aerosols (volcanic ash, biomass burning, anthropogenic pol-  
366 lution) can also affect the signal recorded by MODIS, but we argue that such short-lived  
367 events are smoothed out by the monthly averaging, except where the number of avail-  
368 able records is low. All of the above suggests that the simple proxy used here yields plau-  
369 sible SSAer AOD values derived from MODIS, although the uncertainty on these values  
370 was not quantified in this work.

### 371 3 Results and discussion

#### 372 3.1 Representation of polar SSAer in CMIP6

373 In the Arctic, the CMIP6 1951–2014 climatology of the SSAer surface mass mix-  
374 ing ratio (referred to as *mmrss* from now on) shows maximum values over the northern  
375 Atlantic and northern Pacific (Figure 2), with the mixing ratio decreasing poleward, reach-  
376 ing averages below  $1 \mu\text{g kg}^{-1}$  in the high Arctic. CNRM-ESM is an exception, with mix-  
377 ing ratios more than one order of magnitude greater than any other model. This discrep-  
378 ancy is discussed later on. The northward negative gradient is consistent with an increase  
379 of the relative area fraction covered by sea ice as latitudes increase, which inhibits the  
380 production of sea spray. Over the continents, concentrations are generally below  $1 \mu\text{g kg}^{-1}$ ,  
381 down to less than  $50 \text{ng kg}^{-1}$  in some models, with *mmrss* decreasing inland, in connec-  
382 tion with the deposition of the SSAer during transport. Therefore, all the models have

383 characteristics that are consistent with the expected behavior of SSAer production and  
384 transport patterns.

385 Although the spatial distribution remains relatively consistent (Figure 2), in terms  
386 of magnitude, there is a large diversity between models. CNRM-ESM appears as an out-  
387 lier at both poles, yielding very high  $mmr_{ss}$  of up to  $900 \mu\text{g kg}^{-1}$ , 20 times larger than  
388 any other model. This can be explained by a larger coarse size radius of SSAer at emis-  
389 sion in CNRM-ESM compared to the other models, as already noted in Thornhill et al.  
390 (2021). In this regard, CNRM-ESM being an outlier, this model is not included in the  
391 continuation of the analysis unless explicitly mentioned. CNRM-ESM aside, GISS presents  
392 the highest mixing ratios, with more than  $40 \mu\text{g kg}^{-1}$  in the northern Atlantic and more  
393 than  $1 \mu\text{g kg}^{-1}$  over most of the high Arctic and continental areas. At the other end of  
394 the spectrum, MRI-ESM and MIROC-ES2L do not exhibit mixing ratios above  $10 \mu\text{g kg}^{-1}$ ,  
395 and they drop to less than  $50 \text{ng kg}^{-1}$  over continental areas. This spread in magnitudes  
396 will be further analyzed in Section 3.1.2 based on source functions. In some models, the  
397 latitudinal gradients are sharper (e.g. BCC-ESM compared to EC-Earth) suggesting dif-  
398 ferent representations of atmospheric dynamics (transport, boundary layer dynamics)  
399 and deposition (dry and wet).

400 For the Antarctic (Figure 3), this climatology of  $mmr_{ss}$  has larger values than for  
401 the Arctic, due to the Southern Ocean providing a large source area of sea spray com-  
402 bined with strong winds. A band of maximum  $mmr_{ss}$  is found around  $50^\circ\text{S}$  in the South-  
403 ern Ocean in all the models, followed by a negative gradient toward the pole related to  
404 deposition during the transport. Again, CNRM-ESM aside, GISS presents the highest  
405 values, whereas MRI-ESM and MIROC-ES2L have the lowest, and the poleward gradi-  
406 ent is more or less sharp depending on the model. Similarly to the Arctic, CMIP6 mod-  
407 els give a generally consistent spatial distribution of  $mmr_{ss}$  in the Antarctic, except for  
408 the magnitudes, which are even more diverse.

409 The diversity in spatial gradients between models is particularly relevant for the  
410 interpretation of ice cores from polar ice sheets (Greenland, Antarctica). Sea salt in ice  
411 cores at coastal sites can be used as a proxy for sea ice conditions variability, but mod-  
412 els usually show that for continental polar areas, meteorology, atmospheric transport,  
413 and deposition control sea salt in ice cores instead (Levine et al., 2014; Rhodes et al.,  
414 2018). The differences in transport shown here in CMIP6 models suggest that the rel-  
415 ative attribution of sea salt variability in ice cores to transport meteorology and changes  
416 in the sea ice source can be quite uncertain. The spatial distribution is consistent from  
417 one model to another, but differences in gradient suggest that the representation of at-  
418 mospheric dynamics and sinks (wet and dry deposition) may differ.

419 Figure 4 further summarizes the model diversity, including for other SSAer related  
420 variables. Similarly to mixing ratios, there is a large diversity in total mass emission and  
421 deposition fluxes, which partly accounts for the diversity in  $mmr_{ss}$ . In addition, SSAer  
422 are not found at the same altitudes in all the models. This information is contained in  
423 the aerosol layer height, which is defined as a weighted mean of SSAer layer height us-  
424 ing the  $mmr_{ss}$  of each layer as the weight (Figure 4). For CESM this height is 956 m,  
425 while it is only 136 m in IPSL-CM6. This aerosol layer height is important when it comes  
426 to the interaction of SSAer with clouds. The residence time (or lifetime) of SSAer is one  
427 of the most diverse metric, with values between a few hours up to several days depend-  
428 ing on the model. This factor may explain the differences in transport over land, since  
429 models with longer residence time also feature higher concentrations over Antarctica and  
430 Greenland (Figures 2 and 3). These differences in lifetime can be explained by the ver-  
431 tical distribution of SSAer: models with longer lifetime also have higher aerosol layer height.  
432 GISS is an exception in that case, but the relatively small deposition flux compared to  
433 the other models compensates for the lower aerosol height and extends the residence time.  
434 SSAer optical depth is also diversely represented in the models, and not directly related  
435 to  $mmr_{ss}$ , indicating possible differences in the parameterizations of the size distribu-

436 tion and hygroscopicity. We note that the GISS AOD values for SSAer are much higher  
437 than other models, therefore we exclude this model from the AOD analysis that follows.

438 In summary, there is a large diversity in CMIP6 models in terms of their SSAer cli-  
439 matologies at the poles, from the mass emissions (factor 3 between lower and higher mod-  
440 els) to the surface mass mixing ratios (factor 4-5), through the aerosol layer height (fac-  
441 tor 7-8), lifetime (factor 9), optical depth (factor 4) and total deposition (factor 2-3). In  
442 the Arctic, dry deposition is more diverse (factor 15) than wet deposition (factor 3), whereas  
443 in the Antarctic, both dry and wet deposition have a similar inter-model spread (factor  
444 9). This difference in variability in wet deposition might be related to the difficulty to  
445 properly reproduce Antarctic precipitation in models (Palerme et al., 2017).

### 446 3.1.1 Model diversity drivers

447 The diversity in SSAer climatology is further investigated and explained in terms  
448 of the annual cycle of *mmrss* and the associated drivers (Figure 5). *mmrss* over the ocean  
449 is driven by emissions, the height of the boundary layer, and deposition rates. Emissions  
450 are themselves driven by wind speed and sea ice fraction. SST also affects emissions, but  
451 for consistency this variable is not included in the following analysis on annual cycles of  
452 emission drivers, since only four of the models take it into account in their source func-  
453 tion. Here the focus is on the dynamical drivers and their effects on emissions and con-  
454 centrations. Figure 5 presents the annual cycle of the aforementioned variables for the  
455 Arctic and Antarctic, averaged over grid points where emissions are strictly positive and  
456 the open ocean fraction is at least 10%. This filter is applied to allow a fair comparison  
457 across all models.

458 In the Arctic, mass emissions are consistently at their lowest in the summer months  
459 (Figure 5c), when despite increasing sea ice melt and therefore increasing open ocean area  
460 (Figure 5e), wind speeds are at their lowest (Figure 5g), thus limiting sea spray. All mod-  
461 els show similar magnitudes in summer, except for IPSL-CM6 which features greater val-  
462 ues. The spread is larger in the fall/winter months with a factor of up to three between  
463 IPSL-CM6 and GISS on the total emission rate in October. This diversity in emissions  
464 seems driven mainly by diversity in sea ice (larger spread) and then by wind speed. Fur-  
465 thermore, the source function formulation and size distribution of the emitted aerosols  
466 are key factors that are discussed in Section 3.1.2.

467 For the winter months, when wind speeds are higher, the sea ice fraction seems to  
468 be the factor limiting emissions, while in the fall, when there is more open ocean, the  
469 wind seems to be the controlling factor. In parallel, the ongoing reduction of sea ice cover  
470 in the Arctic appears to be correlated with stronger winds in fall/winter months (Vavrus  
471 & Alkama, 2022). Therefore, in the context of future climate, the shape of the annual  
472 cycle of emissions is likely to change, with possibly an even greater amplitude between  
473 summer and fall/winter emissions. Given that the radiative impact of SSAer changes with  
474 seasons (Section 3.3.1), changes in the seasonality of SSAer emissions might have impor-  
475 tant implications for the polar climate.

476 For the Antarctic (Figures 5d, f, h), the emission drivers are even more spread across  
477 models, particularly the open ocean fraction in the winter months, resulting in a diver-  
478 sity factor of up to 6 in total mass emissions. Unlike for the Arctic, annual cycles show  
479 different shapes in some models. For example, MIROC-ES2L and MPI-ESM show a SSAer  
480 production peak in May–Jun whereas the other models have maximum emissions in Mar–  
481 Apr, along with a sharper seasonality. In this case, the sea ice cover appears to be the  
482 reason for this diversity.

483 The diversity in emissions is partly translated into *mmrss* (Figure 5a, b) although  
484 it does not account for the relative ranking of the models or for some characteristics of  
485 the annual cycle. For example, GISS is the model with the lowest mass emissions in the

486 Arctic (Figure 5c), and around median emissions in the Antarctic (Figure 5d), but shows  
487 the highest mixing ratios at both poles. This could result from the representation of the  
488 dynamics of the boundary layer, since GISS has a mean planetary boundary layer height  
489 between 300 to 500 m, about three times lower than other models (Figure 5i, j), which  
490 results in a higher boundary layer concentration for the same amount of emissions. EC-  
491 Earth also shows very shallow boundary layer heights similar to those of GISS, along with  
492 a comparatively higher emission rate at both poles, which should result in mixing ratios  
493 higher than in the other models. However, those mixing ratios are lower, due to a shorter  
494 lifetime of SSAer of around 14 h, while it is more than a day in GISS (Figure 4). This  
495 is also reflected by a deposition flux twice as large in EC-Earth compared to GISS, where  
496 the difference mostly comes from dry deposition (Figure 4). In terms of the annual cycle,  
497 in the Arctic the seasonality of the boundary layer height shows the same shape as  
498 for emissions, which are both consistent across models. Therefore, the cycle of mixing  
499 ratio follows the cycle of emissions. However, in the Antarctic, the planetary boundary  
500 layer height cycle is more diverse, as is the case for emissions, resulting in more diverse  
501 values and seasonality. Deposition fluxes and lifetimes further modify the relative ranking  
502 of models in terms of mixing ratio as shown in Figure 4, but the seasonality is not  
503 affected.

### 504 3.1.2 Role of emission source functions

505 The source function formulations also affect the diversity in emissions. Figure 6  
506 explores the differences in fluxes resulting from the diversity of source functions used in  
507 the CMIP6 models. The source functions and aerosol modes/bins used in the models are  
508 summarized in Table 1. All the models except NorESM use a whitecap fraction approach  
509 based on surface wind speed, but not all include a dependence on SST. Instead, NorESM  
510 uses the air-entrainment-based Salter et al. (2015) formulation.

511 Figure 6a shows the theoretical mass flux from an offline calculation of SSAer emis-  
512 sions for each source function using an arbitrary fixed wind speed and SST ( $10 \text{ m s}^{-1}$  and  
513  $5^\circ\text{C}$ , respectively) and varying aerosol size bins, as described in Section 2.1. Figure 6b  
514 explores the effect on this flux of varying wind speed and SST for given size bins. Some  
515 CMIP6 models use a modal aerosol approach, some use a sectional (size bins) aerosol  
516 approach. Here, for the sake of comparability of the source functions, we use a sectional  
517 approach for the aerosol sizes. Therefore, the following analysis reflects the model diversity  
518 due to the source functions without considering the actual aerosol size distributions  
519 (modal or sectional) that are included within each model.

520 Figures 2 and 3 show that CNRM-ESM has  $mmr_{ss}$  much higher than all the other  
521 models. This is explained by the use of the Grythe et al. (2014) source function with size  
522 bins up to  $20 \mu\text{m}$  radius. First, the other CMIP6 models only emit up to a maximum radius  
523 of  $\sim 10 \mu\text{m}$ , so CNRM-ESM adds an extra mass in the  $10 \mu\text{m}$ – $20 \mu\text{m}$  range. Second,  
524 the Grythe et al. (2014) source function has a coarse emission mode with a mean radius  
525 of  $30 \mu\text{m}$ , inducing large emissions of coarse particles which strongly contribute to mass.  
526 Figure 6a shows that for a maximum radius of  $20 \mu\text{m}$ , this source function yields a mass  
527 flux one order of magnitude greater than any other model for a given wind speed of  $10 \text{ m s}^{-1}$   
528 and  $5^\circ\text{C}$  SST, which is the difference observed in Figure 4.

529 Figure 6a also shows that for a given choice of aerosol size bins (assuming a sectional  
530 approach with mean radii  $0.05$ – $0.5$ – $1$ – $R_{max} \mu\text{m}$  and varying  $R_{max}$ ), selecting a source  
531 function over another can change the flux by up to one order of magnitude (e.g. grey bar  
532 for JA11 versus grey bar for GR14). Furthermore, the source functions do not have the  
533 same sensitivity to the choice of the larger aerosol size. Some source functions are very  
534 sensitive to the radius of the coarser section, which leads to large changes in the mass  
535 flux (SM98, MA06 and GR14) with larger mass emissions for bigger particle bins. But  
536 for the others, the number flux for larger particles decreases fast which causes the mass

537 flux to increase less as radii increase. For the SSAer emissions, although it is critical for  
538 the wind speed (and SST when used) to be accurately represented, the diversity between  
539 models is driven primarily by the choice of the source function formulation and aerosol  
540 size bins rather than by meteorological differences (see Figure 6a and Figure 6b). When  
541 changing wind speeds by  $\pm 1 \text{ m s}^{-1}$  (which is the spread found in CMIP6 models), the  
542 impact on the mass emission flux is generally smaller than a change in the coarse mode  
543 aerosol size bins. Figure 6b also shows the influence of accounting for SST in the source  
544 function (blue and green stars). In general, changing the SST by  $\pm 5^\circ\text{C}$  leads to a sim-  
545 ilar to smaller change in the mass emission flux than varying the wind speed by  $\pm 1 \text{ m s}^{-1}$ .  
546 Since the spread in SST in CMIP6 models is less than  $5^\circ\text{C}$ , we therefore conclude that  
547 the emission flux dependence on SST is not an important contributor to the CMIP6 model  
548 diversity.

549 The fine aerosol size bins (taken here as 300 nm and smaller aerosol diameter) in-  
550 fluence the number of SSAer potentially acting as CCN. BCC-ESM barely produces any  
551 SSAer below 300 nm since the smaller aerosol bin considered has a minimum diameter  
552 of 200 nm. For the other source functions, we compute the number emission flux con-  
553 sidering the following SSAer diameter bins: [30-40-50-60-70-80-90-100-200-300] nm. In  
554 this range of diameters, the total number flux of SSAer varies by a factor of 8, except for  
555 the MO86 function which yields a number flux 2 orders of magnitude larger in this size  
556 range. Therefore, for models including the interactions of aerosols with radiation and clouds,  
557 the choice of source function can strongly influence the associated radiative impacts, as  
558 illustrated in Prank et al. (2022).

559 In summary, the large variety in the magnitude of simulated SSAer concentrations  
560 at the poles is driven primarily by the choice of aerosol emission sizes and the source func-  
561 tion, and secondly by the meteorological drivers of emissions (open ocean fraction, wind  
562 speed, mean planetary boundary layer height). The atmospheric processes (deposition,  
563 transport, ageing) and thereby the residence time of SSAer drives the differences in spa-  
564 tial distribution and concentrations over the ocean and land. The variety in seasonal-  
565 ity is primarily driven by sea ice and meteorology, with diverse sea ice concentration and  
566 wind speed annual cycles modulating emissions, but also heterogeneity in the represen-  
567 tation of the planetary boundary layer and deposition which influence concentrations ir-  
568 respective of the emission flux. The choice of aerosol sizes and source function formu-  
569 lation also affects the number of SSAer that could act as CCN.

## 570 3.2 Evaluation using observations

### 571 3.2.1 Comparison with ground based stations

572 Given the previously identified diversity in *mmrss* in the investigated CMIP6 mod-  
573 els, a comparison with the observed sodium aerosol concentration from ground-based sta-  
574 tions is conducted to evaluate individual model and ensemble performance (Figure 7, Fig-  
575 ure 8 and Figure A2). Figure 7 summarizes the comparison between the annual cycle  
576 of sodium near-surface concentration in the CMIP6 models and the measurements for  
577 the 14 stations. The NMB and correlation of the annual cycle of individual models as  
578 well as the ensemble mean are computed. Reanalysis data from MERRA2 and CAMS  
579 are also included. The data from observations and models are averaged over the longest  
580 available period for each of them, i.e. 1951–2014 for CMIP6, 1980–2021 for MERRA2,  
581 2003–2021 for CAMS, and as indicated in Figure 1 for the measurements. A compar-  
582 ison (not shown here) was performed to test the validity of considering various time pe-  
583 riods in the evaluation against observations. For the 4 stations which have data for the  
584 common period 2003–2014, all data sets including measurements, CMIP6 models and  
585 reanalysis were limited to the 2003–2014 period and the same comparisons were made.  
586 This analysis revealed that the changes in values are minor and the conclusions about

587 the annual cycles are not affected by a change in the time period considered, hence val-  
588 idating the approach using the longest time periods available.

### 589 *Arctic*

590 For the Arctic stations, Figure 7 shows that most CMIP6 models have mean con-  
591 centrations around two to eight times larger than observations. Except for one station  
592 where it is negative, the correlation between the modeled and observed annual cycles of  
593 concentrations are positive, and mostly above 0.5, indicating a reasonable seasonality.  
594 At the Irafoss and Summit stations, the correlation coefficient between the CMIP6 en-  
595 semble mean annual cycle and the observations is high, at 0.85 and 0.84, respectively,  
596 despite NMB of up to one order of magnitude in individual models. At the Zeppelin, Utqiagvik,  
597 Pallas, Karasjok and Breckkälén stations, NMB and correlations are between 91% and  
598 435%, and 0.61 and 0.81, respectively. Unlike the two previous ones, some models at these  
599 four stations are not significantly correlated with the observations at the 95% level. Alert  
600 and Villum stations are the only two locations where the NMB is relatively small, and  
601 negative (around -20%). However, due to the low correlation (-0.45 at Alert, 0.44 at Vil-  
602 lum), this relatively low NMB is not a sign of good performance, as discussed later.

603 In order to understand if the variation by season for SSaer is correctly represented  
604 we apply a bias correction on CMIP6 model output (Figure 8). For each model, the an-  
605 nual cycle is adjusted by the factor  $\langle \text{OBS} \rangle / \langle \text{MODEL} \rangle$ , which is the annual mean ob-  
606 served sodium concentration divided by the annual mean in the model for each station.  
607 Using the bias corrected data (Figure 8) for the Arctic stations Alert and Villum, CMIP6  
608 models have very diverse annual cycles (the median correlation across models is not sig-  
609 nificant at the 90% level). The ensemble mean has no significant correlation with the cor-  
610 responding observations at the 95% level (boundaries of the confidence interval have op-  
611 posite signs). Also, the yearly maximum in Aug–Sep in the models contrasts with ob-  
612 servations which are at their minimum during that period. For such high-latitude sta-  
613 tions, where the Arctic Ocean is covered with sea ice throughout the year and the pro-  
614 duction of sea spray does not occur, it is thought that the observed wintertime SSaer max-  
615 imum originates from blowing snow on sea ice emissions (Yang et al., 2008; J. Huang &  
616 Jaeglé, 2017; Yang et al., 2019) or from sea spray originating from leads (Held et al., 2011;  
617 Kirpes et al., 2019). In CMIP6 models, these sources are not included in the parame-  
618 terizations, which may explain the lack of correlation with observations at Alert and Vil-  
619 lum and the negative NMB in wintertime. However, some models (UKESM and HadGEM)  
620 seem to have the right seasonal cycle at Alert, without including a sea ice source of SSaer.  
621 Additional analyses show that the emissions surrounding the location have a minimum  
622 in winter, but the annual cycle of planetary boundary layer height varies more with sea-  
623 son in UKESM and HadGEM compared to the other models, with higher values in sum-  
624 mer and shallower heights in winter (see Figure A3). This explains the shape of the an-  
625 nual cycle despite the absence of winter local sources in the models. Since winter sources  
626 such as blowing snow are observed in measurements (Frey et al., 2020), these two mod-  
627 els likely have the right annual cycle for the wrong reasons. Except at Utqiagvik where  
628 the Dec–Jan high concentrations are missed by the models, the seasonality is reasonably  
629 well captured by the ensemble mean at the other locations.

630 An underestimate of poleward transport of SSaer could also account for the seem-  
631 ingly smaller bias at higher latitude and a build up of concentrations at lower latitude.  
632 This hypothesis is difficult to test within the framework of this study, and would require  
633 including additional measurement stations to decrease the likelihood of a sampling bias.

### 634 *Antarctic*

635 For Antarctic stations, the magnitudes of the NMB are similar to those of the Arc-  
636 tic sites, except at Dumont d’Urville and Neumayer where several models have a rela-

637 tive NMB below 100% (Figure 7). The diversity between models is large as well, with  
638 no significant across-model correlation at the 90% level for any station, and a strictly  
639 positive correlation at the 95% level of the ensemble mean with observations only at Du-  
640 mont d’Urville and Palmer stations (Figure 8). At Concordia station, two models ex-  
641 hibit an Arctic-like cycle with maximum concentrations in Dec–Feb (MRI-ESM and MIROC-  
642 ES2L), while the others produce an annual cycle with maximum concentrations in Jun–  
643 Aug. In both groups, the clear maximum recorded by measurements in November is missed.

644 The models are relatively good at the coastal site of Dumont d’Urville, with a 0.64  
645 correlation and a bias corrected annual cycle mostly within one standard deviation of  
646 the observations (Figure 8). In contrast, at Concordia station which is 1200 km further  
647 inland from Dumont d’Urville (Figure 1), the correlation with observations is not sig-  
648 nificant at the 95% level and not one individual model is within one standard deviation  
649 of the measurements. This difference in performance might be indicative of inadequate  
650 removal processes over land. In particular, climate models at a resolution lower than 1°  
651 tend to underestimate precipitation over Antarctica (Tang et al., 2018), which would re-  
652 sult in too low wet deposition along transport, and therefore too high concentrations over  
653 the continent, despite reasonable concentrations at the coast. In addition, the orogra-  
654 phy of this region might not be well reproduced in climate models, which could lead to  
655 inadequate dynamics and thus explain the shortcomings in CMIP6 in terms of the an-  
656 nual cycle of SSaer.

657 At Halley station, the comparison is partially hindered by the relatively short length  
658 of the observation records, which only cover 3 years and comprise a large variability, but  
659 the CMIP6 bias-corrected values are mostly within one standard deviation of the obser-  
660 vations for this station (Figure 8). At Neumayer station, the shape of the annual cycle  
661 in the models is reasonable but is shifted two months too early compared to measure-  
662 ments. At Dumont d’Urville, all models adequately produce a maximum in Dec–Feb, al-  
663 though generally too high compared to observations and possibly one month late, which  
664 leads to a distorted seasonal cycle. A similar comparison can be made for Palmer sta-  
665 tion, although with a maximum delayed by two months compared to Dumont d’Urville.  
666 These two latter stations are the lower latitude ones (north of 70°S) where the sea ice  
667 maximum extent in winter is lower according to Figure 1. Like for the Arctic, the ab-  
668 sence of a sea ice related SSaer source in the models (blowing snow, leads) degrades their  
669 performance during winter.

### 670 *Reanalyses*

671 Two reanalysis data sets are also included in this analysis (Figure 7) and compared  
672 to observations. MERRA2 is known to have a positive bias on SSaer mass concentra-  
673 tion of around one order of magnitude even at lower latitudes (Kramer et al., 2020), which  
674 was partly attributed to a distortion of the size distribution of SSaer, with too few small  
675 particles and too many large ones (Bian et al., 2019). This is consistent with Figure 7  
676 where MERRA2 is found to systematically overestimate concentrations with a larger pos-  
677 itive NMB than the CMIP6 ensemble mean, for both poles, between 163% and 2,532%.  
678 CAMS has a generally better performance than MERRA2, both in terms of correlation  
679 and NMB, the latter being limited to 730% at most. Generally speaking, CAMS is less  
680 biased than the CMIP6 ensemble, but has a lower correlation when it comes to repro-  
681 ducing the observed annual cycle. These two comparisons show that despite being com-  
682 monly used as validation data sets, reanalyses have difficulties in reproducing observed  
683 SSaer concentrations at the poles, and have a generally poorer performance than the CMIP6  
684 ensemble. However, since SSaer concentrations are not assimilated in these reanalyses,  
685 and AOD is assimilated only as total AOD, a better performance than CMIP6 was not  
686 expected.

### 3.2.2 Comparison of modeled SSAer AOD with MODIS AODss

AOD is often used to evaluate aerosols in climate models, since it is closely related to the full aerosol burden throughout the atmospheric column, including the impact of water uptake on aerosols. It is also more closely related to direct aerosol-radiation climate forcing than surface observations, and is less sensitive to errors in vertical aerosol distributions. SSAer AOD at 550 nm is provided for a subset of CMIP6 models including BCC-ESM, EC-Earth, IPSL-CM6, MPI-ESM, MRI-ESM, NorESM, and compared here to AODss at 550 nm extracted from MODIS Dark Target/Deep Blue satellite data (Figure 9). The monthly MODIS data are processed as described in Section 2.2.2 to approximate the contribution of SSAer to total AOD, noting that AOD is not available for cloud covered regions and ice/snow covered surfaces. MODIS data is also scarce during the polar night due to the absence of visible light. MODIS Terra and MODIS Aqua AODss are shown separately due to the differences between these two monthly AOD products (Sogacheva et al., 2020).

Figure 9 shows the magnitudes and spatial patterns of SSAer AOD in CMIP6 and AODss in MODIS, for the Arctic and the Southern Ocean. In the northern Atlantic, the CMIP6 ensemble median is around 0.02 (0.04, respectively) higher than MODIS Terra (Aqua, respectively). Spurious high AODss values in satellite data over the high Arctic (brown pixels in Figure 9 middle with AODss up to 1 on average) could be artifacts related to the scarcity of valid records available in the region (due to possible cloud contamination or poor snow/sea ice screening) making the comparison more difficult. For the Antarctic, values south of 60°S are comparable between CMIP6 SSAer AOD and MODIS AODss, below 0.02 in coastal regions with a positive northward gradient up to around 0.08 at 60°S. However, in the area between 50°S and 60°S, the band of maximum SSAer AOD in CMIP6 is not observed in the AODss MODIS data (Terra or Aqua), except for sporadic hot spots. For this area, the spatial distribution in MODIS is less homogeneous and has a lower AODss on average compared to CMIP6. Given the semi-permanent presence of clouds at these latitudes, around 90% annually (Lachlan-Cope, 2010), a sampling bias in the MODIS data cannot be excluded to account for this discrepancy, which does not invalidate the high values in CMIP6.

The spatially averaged SSAer AOD and AODss show reasonable agreement between CMIP6 and MODIS in terms of the annual cycle (Figure 9 right). For the Arctic, MODIS features a late winter (Feb–Mar) maximum in AODss that is not represented in the models, whereas most models have a maximum SSAer AOD in early winter (Dec–Jan) that is not found in MODIS and up to 0.1 higher than the MODIS values. However, for those winter months (Nov–Feb), the MODIS data are more sparse than in summer (Jun–Sep), which could result in another sampling bias (Figure 9 right - grey bars). Since cloud cover is lower in winter compared to summer (Eastman & Warren, 2010), and should therefore impede AOD retrieval less often, sea ice cover can explain the lack of records, in combination with the polar night. Sea ice is at its maximum extent and is too bright a surface for MODIS instruments to accurately separate the contribution to back-scattering from the ground and from aerosols (Mei et al., 2013), leading to fewer valid records in winter than in summer. On the other hand, the MODIS-derived annual cycle of AODss is quite similar to the cycle of total aerosol mass and surface area observed in Tunved et al. (2013), which could indicate limitations in our AODss extraction approach. Similarly, the scarcity of MODIS data in the Antarctic for Mar–Sep prevents such a comparison. Furthermore, the observed decrease in AODss in Apr–May could be due to a sampling bias, since MODIS records are less numerous south of 60°S compared to other months (Figure 9 - grey bars). For the austral summer months (Nov–Feb), when the comparison is less uncertain due to a larger number of available records, all the models are within one standard deviation of both MODIS Terra and Aqua values and closer to the Aqua mean. This is true for all the models in the Arctic, and most of them in the Antarctic.



739 tic. The shape of the monthly variations is reasonably well reproduced in both cases, except  
740 in winter.

741 The CMIP6 ensemble is closer to MODIS Terra when it comes to climatological  
742 maps, but closer to MODIS Aqua for the summer months, when the comparison is more  
743 robust thanks to a larger number of MODIS records. The offset of around 0.02 obtained  
744 here between MODIS Aqua and MODIS Terra in our AODss product is well known and  
745 described in the literature, in which MODIS Aqua is considered to be more accurate than  
746 MODIS Terra (Sogacheva et al., 2020). Therefore, the better agreement of CMIP6 mod-  
747 els with MODIS Aqua in summer is an indication that the SSAer AOD is reasonably cap-  
748 tured in the CMIP6 models, although the model variability is large for the winter months.

749 Despite the fairly large discrepancies in *mmrss* revealed in Section 3.2.1, the SSAer  
750 AOD at 550 nm shows better performance in the CMIP6 models compared to the satel-  
751 lite data. This indicates that the direct radiative effect of SSAer is likely well reproduced  
752 for the poles as well. This also suggests, given the bias on surface mass concentrations,  
753 that (i) the size distribution of SSAer might not be adequate, possibly steered toward too  
754 coarse particles, or (ii) that the vertical distribution of SSAer is biased and accumulates  
755 too much mass at the surface. However, the good performance in SSAer AOD is not nec-  
756 essarily a sign of adequate fine mode number concentrations. Some models are known  
757 to have hygroscopic growth factors that are too high (Burgos et al., 2020), which can in-  
758 crease SSAer AOD despite incorrect (too low) quantities of fine fraction mode particles.  
759 Although this is not analyzed further in this work, compensating effects between num-  
760 ber, size and hygroscopicity of SSAer needs further investigation in the future.

### 761 3.3 Implications for our understanding of polar climate

762 In this section we address the implications of the diverse representation of SSAer  
763 in CMIP6 for our understanding of present and future climate. In what follows, we first  
764 evaluate the sensitivity of the polar climate to SSAer based on the CMIP6 *piClim-2xss*  
765 experiment. Then, historical and future trends of SSAer emissions and *mmrss* are inves-  
766 tigated under scenarios SSP126 and SSP585 to assess the uncertainty borne by climate  
767 projections owing to SSAer.

#### 768 3.3.1 Radiative impact of SSAer

769 The pre-industrial climate experiments from the AerChemMIP activity provide a  
770 control (*piClim-control*) and a doubled SSAer emission (*piClim-2xss*) experiment, for a  
771 30 year period under 1850 climate conditions. Three CMIP6 models provide the top-of-  
772 the-atmosphere net downward radiative flux (*rtmt*) for these experiments and are used  
773 in this section. The change in *rtmt* between the *2xss* and *control* experiments is used  
774 here to evaluate the radiative impact of SSAer. The entire 30 year period is considered.  
775 For the three models considered, this includes the aerosol-radiation interaction and the  
776 aerosol-cloud interaction, although they cannot be disentangled, since *rtmt* provides to-  
777 tal radiation only (short-wave + long-wave). The *piClim* simulations are fixed-sst, so that  
778 *rtmt* includes the effect of rapid atmospheric adjustments, but not the effect of climate  
779 feedbacks from long-term surface temperature change. In this respect, the *rtmt* change  
780 is comparable to an effective radiative forcing.

781 One important factor for the direct and indirect radiative effects of SSAer is their  
782 vertical distribution. We show the diversity in the vertical distribution of both SSAer and  
783 clouds in Figure A4 for ocean/ice covered regions north/south of 60°N/S. There is a large  
784 diversity between modeled profiles, of more than two orders of magnitude above 5,000 m  
785 altitude for SSAer, and a factor of around 10 in clouds throughout the column. This sug-  
786 gests that the radiative impact of SSAer can also be assumed to be very diverse and un-  
787 certain.

788 Figure 10 shows the average change in  $rtmt$  between the doubled SSAer emissions  
789 and the control experiment, for summer months and winter months in the Arctic and  
790 Antarctic. In summer, when sea ice extent is at its minimum in the Antarctic, the ra-  
791 diative impact of SSAer is mostly negative (cooling effect) in the three models over the  
792 ocean, with up to  $-10 \text{ W m}^{-2}$  in NorESM and  $-5 \text{ W m}^{-2}$  in IPSL-CM6 and UKESM (Fig-  
793 ure 10). This important change is probably partly related to the aerosol-cloud interac-  
794 tion and its albedo effect over darker surfaces (open ocean), as found in Struthers et al.  
795 (2011). The aerosol direct effect also likely contributes to this change, especially in NorESM  
796 where the change in AOD is large over the Southern Ocean, with more than  $+0.25$  on  
797 average (Figure A5). Such an important change is not found in the other models for the  
798 Southern Ocean (less than  $+0.1$ ), explaining why the cooling effect is larger in NorESM  
799 in summer in the Antarctic than in IPSL-CM6 and UKESM.

800 Over the Antarctic continent in summer, for most areas the radiative impact can-  
801 not be significantly distinguished from zero at the 90% level according to a Wilcoxon test,  
802 but regionally averaged south of  $60^\circ\text{S}$ , a negative radiative impact significant at the 95%  
803 level is found, comprised between  $-0.34 \pm 0.02 \text{ W m}^{-2}$  and  $-1.01 \pm 0.07 \text{ W m}^{-2}$  (Table 2).  
804 In winter, when sea ice extent is larger and there are fewer areas prone to sea spray pro-  
805 duction in the region, the radiative impact is slightly positive in West Antarctica but mostly  
806 not significantly different from zero at the 90% level in the region when considering all  
807 three models (Figure 10 and Table 2).

808 NorESM and UKESM indicate a cooling effect in the high Arctic in winter, with  
809 a regionally significant negative radiative impact at the 95% level (Table 2). IPSL-CM6  
810 suggests a small heating effect in northeastern Canada and a slight heating in the high  
811 Arctic for Dec–Feb, although the regional average is smaller than the cooling obtained  
812 in the other models. In summer, the changes are stronger and more heterogeneous, with  
813 regions of large cooling next to regions of large heating, although generally not signif-  
814 icant at the 90% level (Figure 10), resulting in a regionally weak cooling effect overall  
815 in all the models (Table 2). The weak change in AOD in summer can partially explain  
816 this moderate radiative effect (Figure A5).

817 The effects of doubling SSAer can be further described in terms of changes in air  
818 surface temperature ( $tas$  variable in CMIP6), as shown in Figure A6. NorESM predicts  
819 a warming in the winter both in the Arctic and Antarctic ( $+0.20^\circ\text{C}$  and  $+0.17^\circ\text{C}$ , re-  
820 spectively), while the response in the other models is either a slight cooling or warming,  
821 but one order of magnitude smaller. In the summer, models agree on a cooling effect in  
822 the Arctic ( $-0.013^\circ\text{C}$  to  $-0.078^\circ\text{C}$ ), while the sign of the change is uncertain in the Antarc-  
823 tic (the average of the three models shows a zero net change). In the winter, these changes  
824 in temperature are equally driven by oceanic and land regions, whereas in the summer  
825 the temperature change is mainly found above land. This may be related to the more  
826 homogeneous surface albedo in winter when sea ice extent is large and land is covered  
827 in snow, whereas in summer the heat capacity of the open ocean contrasts with that of  
828 the land. These changes in surface temperature are not directly connected to the changes  
829 in top-of-the-atmosphere radiation found in Table 2, particularly in the Antarctic where  
830 the large summer decrease in radiation in NorESM ( $-1.01 \text{ W m}^{-2}$ ) yields a surface warm-  
831 ing of  $+0.065^\circ\text{C}$ . Cooling/heating effects over land/ocean which have different heat ca-  
832 pacity and albedo may be at play in this case. The vertical distribution of the changes  
833 in radiation may also play a role.

834 Figure A6 also shows the same change in surface temperature but in the *piClim-*  
835 *2xdust* experiment, where dust emissions are doubled, instead of SSAer. In the Antarc-  
836 tic, both species have similar impacts on surface air temperature (very limited in sum-  
837 mer months, slight warming in winter months, on average). In the Arctic, dust have a  
838 cooling effect in winter, of the same magnitude as the warming induced by SSAer, whereas  
839 in summer, the cooling from SSAer is one order of magnitude larger than the cooling from  
840 dust. The changes are also more widespread around zero in the case of SSAer, with wider

841 distributions than for dust, suggesting a greater sensitivity to SSAer than dust. Com-  
842 pared to SSAer, dust has limited local sources at the poles and mostly comes from long-  
843 range transport, which explains its smaller regional impact. However, this comparison  
844 speaks to the relevance of evaluating more closely SSAer and their climate impacts at the  
845 poles, which are comparatively less studied than for dust.

846 The implications of the previous analyses are not straightforward, since the *piClim*  
847 experiments consider pre-industrial atmospheric conditions, free of the current anthro-  
848 pogenic background. Although polar regions remain relatively pristine areas, they are  
849 affected by the transport of anthropogenic emissions from lower latitudes through warm  
850 air mass intrusions (Li & Barrie, 1993; Quinn et al., 2002; Dada et al., 2022). The non-  
851 linearity of aerosol-cloud interactions (Gryspeerd et al., 2019) requires an adequate aerosol  
852 background, including anthropogenic sources, to obtain reasonable estimates of the in-  
853 direct effect of SSAer emissions and therefore its radiative impact. Furthermore, the ra-  
854 diative impact depends not only on the proper representation of the number and sizes  
855 of SSAer, but also on their hygroscopicity, particularly for the direct effect (Zieger et al.,  
856 2017), which are quite uncertain according to Section 3.1.

857 The relatively strong effect on radiation of doubled SSAer emissions puts Figures 2,  
858 3 and 5 into perspective: the difference in SSAer emissions between two models can be  
859 up to a factor of 4, which according to Figure 10 should mean that the resulting radi-  
860 ative budget at the poles could differ by up to  $2 \text{ W m}^{-2}$  (depending on the season and the  
861 model). This suggests that the uncertainty on the polar radiative budget related to SSAer  
862 within CMIP6 models could have the same magnitude as the 20<sup>th</sup> century increase in  
863 global radiative forcing (Myhre et al., 2013). These numbers are in line with those from  
864 Struthers et al. (2011), where a 23% increase in SSAer AOD in the Arctic is estimated  
865 to result in a  $-0.2$  to  $-0.4 \text{ W m}^{-2}$  radiative impact.

### 866 3.3.2 Historical and future trends

867 As a result of polar amplification, the polar climate is changing even more dramati-  
868 cally than the global climate. Given the connection of sea spray emissions with sea ice  
869 and atmospheric dynamics (e.g. wind speed), significant trends can be anticipated in SSAer  
870 both in present day and future scenarios. These are investigated using ScenarioMIP ex-  
871 periments SSP126 and SSP585 (O'Neill et al., 2016). The analysis conducted hereafter  
872 is restricted to the six CMIP6 models that provide *mmrss* in both scenarios, namely GISS,  
873 HadGEM, MIROC-ES2L, MRI-ESM, NorESM and UKESM. We note that observations  
874 do not have long enough time series to compute multidecadal trends for validation pur-  
875 poses.

876 In the historical period 1951–2014, the mass emission flux of SSAer in the polar re-  
877 gions generally increased and comparatively more homogeneously in the Southern Ocean  
878 than in the Arctic (Figure 11 top). In the latter region, emissions increased more strongly  
879 in the Barents Sea and Greenland Sea, at a rate of up to +6% per decade. In the high  
880 Arctic, this trend is lower, between +1.5% and +3% per decade, with no trend between  
881  $-60^\circ\text{E}$  and  $-180^\circ\text{E}$ . In the Southern Ocean the increasing trend is more homogeneous, be-  
882 tween +1.5 and +6% per decade in most of the area. For the Arctic and Antarctic, the  
883 historical trend is mainly driven by sea ice retreat, although a slight increase in wind speed  
884 is also found in the Antarctic (Figure A7). This Antarctic increase in SSAer is consis-  
885 tent with the findings of Korhonen et al. (2010). To some extent, the difference in trends  
886 of wind speed between the Arctic and Antarctic might be related to an asymmetry in  
887 the trends and dynamics of stratospheric ozone depletion (Turner et al., 2009).

888 The spatially averaged time series of the yearly surface *mmrss* (Figure 11) show  
889 different behaviors between the two poles over the historical period and in the two fu-  
890 ture scenarios SSP126 and SSP585. In the Arctic, in scenario SSP585, each individual  
891 model features an increasing trend resulting in the multiplication of surface *mmrss* by

892 a factor of 1.75 to 2.8 in 2099 compared to the 1951–1971 average (hereafter referred to  
893 as baseline). In the ensemble mean, this increase is by a factor of 2.2. In the SSP126 sce-  
894 nario, three models show a stabilization after 2050 and a slight decrease at the end of  
895 the century. The two remaining models feature a stronger increase, lasting until the end  
896 of the century and reaching levels comparable to those obtained in some models in SSP585.  
897 The associated ensemble mean stabilizes at just under a 1.5 increase at mid-century com-  
898 pared to the baseline. These trends mirror the trends in Arctic sea ice in the CMIP6 mod-  
899 els analyzed in Notz and SIMIP Community (2020), showing decreasing sea ice cover un-  
900 til 2050, followed by a stabilization in SSP126 and a continuous decrease until the end  
901 of the century in SSP585. As a result, differences in trends in individual models might  
902 come from differences in their underlying sea ice evolution. In the Antarctic, the SSP585  
903 trajectory is similar to that in the Arctic, except for a smoother increase, by no more  
904 than a factor of 2 in the more extreme model. Contrary to the Arctic, the increasing trend  
905 in *mmrss* starts in the 1980s, and the SSP126 and SSP585 trajectories start separating  
906 only around the year 2030, after which *mmrss* reaches a plateau in SSP126 until the end  
907 of the century. For both poles, NorESM, which is the only model in this analysis that  
908 includes an SST dependence in its sea spray source function, and which is not based on  
909 a whitecap approach, shows the smallest increase in concentration at the end of the cen-  
910 tury, in SSP126 and SSP585. This is consistent with Figure 6 which showed that for in-  
911 creased SST, the SSAer mass flux decreases in the SA15 source function. As a result, in  
912 a warming climate, accounting for the increase in SST decreases the SSAer mass flux at  
913 the poles compared to not accounting for it. Generally speaking, the trends in all the  
914 models are marginally larger in winter than in summer. For comparison, mid-latitude  
915 oceans do not show historical or future trends in *mmrss*.

916 In addition to following different trajectories, future trends in surface *mmrss* in the  
917 Arctic and Antarctic also have a different spatial distribution, although in both cases a  
918 slight negative trend is found over land in Greenland and the Antarctic continent (Fig-  
919 ure A8). This negative trend over land can be explained by increasing precipitation, and  
920 therefore decreased aerosol residence time, in SSP scenarios in the Arctic (McCrystall  
921 et al., 2021) and over Antarctica (Tewari et al., 2022). All of the Arctic Ocean where sea  
922 ice can currently be found features a strong decreasing trend in sea ice concentration (Fig-  
923 ure A8), which explains the strong increasing trend in *mmrss* in scenario SSP585. In con-  
924 trast, the trend in the Antarctic is mainly driven by increasing *mmrss* in the Belling-  
925 shausen Sea, and marginally by localized spots in the Wedell Sea, which appear to be  
926 sea ice driven (Figure A8).

927 A multiplication of SSAer mass emissions in the Arctic by 3 in SSP585 (as indicated  
928 by the CMIP6 ensemble mean) could imply a regionally negative radiative impact of around  
929  $-1 \text{ W m}^{-2}$  to  $-2 \text{ W m}^{-2}$  in winter at the end of the century based on Section 3.3.1 (see  
930 Figure 10 and Table 2). In particular, UKESM that showed a high sensitivity to dou-  
931 bled SSAer emissions (Table 2) is also the model with the largest future trends in sce-  
932 nario SSP585. The limited emission trend in the Antarctic, including in SSP585, sug-  
933 gests a smaller counteracting effect of SSAer on polar warming. Nevertheless, these changes  
934 in mass emissions do not necessarily translate into a similar change in number of SSAer,  
935 and the latter can have a large impact on the indirect effect of SSAer. No information  
936 on the change in number of aerosols is available in CMIP6 models to further investigate  
937 these future trends in radiative effect, making them quite uncertain.

## 938 4 Conclusions and Perspectives

939 This work evaluates the representation of SSAer in polar regions within CMIP6 in-  
940 cluding a comparison to surface station observations and satellite AOD. Implications for  
941 the radiative balance at the poles in the present-day and future climate are also inves-  
942 tigated. We address the questions:

*How diverse are SSAer emissions/concentrations at the poles in CMIP6 models?*

The inter-model comparisons result in the same conclusions for the Arctic and Antarctic, with a large diversity (up to a factor of 5) in the magnitude of simulated surface mass concentration of SSAer. The spatial distribution is generally consistent between models although the amount of SSAer transported over land varies. Diversity is also important in emissions (factor 3), aerosol layer height (factor 7-8), lifetime (factor 9), optical depth (factor 4) and total deposition (factor 2-3), resulting in a generally uncertain SSAer budget at the poles in CMIP6.

*What are the drivers of this model diversity?* The model diversity in CMIP6 is driven by differences in the sea spray source function formulations and by the drivers of sea spray emission (wind speed, sea-ice cover). We also show large differences in residence time which affect the transport of SSAer and are responsible for model diversity over land. Other SSAer related variables such as AOD, aerosol layer height and deposition fluxes are also diversely represented. We show that even if the emissions were identical, the surface mixing ratio of SSAer would still be different due to different treatments of boundary layer dynamics, aerosol models (micro-physics, treatment internal/external mixing, hygroscopicity, size bins/modes), and deposition fluxes of the SSAer.

*How well do the CMIP6 models represent SSAer at the poles relative to surface observations and remote sensing?* The evaluation of the modeled surface concentrations of sodium mass against ground station observations shows there is a large positive bias of up to one order of magnitude in CMIP6 models. Once the mean bias is corrected, the seasonal variations of SSAer concentration are relatively well captured for lower-latitude stations. For high-latitude stations, there is a deformation of the annual cycle in models compared to observations. The absence of wintertime local sources of SSAer such as blowing snow over sea ice and emissions from open leads can be one reason for that. Possible biases in sea ice representation could also be responsible. Models that include a SST dependence in the SSAer source function are not less biased than ones that do not, because the effect of SST change is smaller than other sources of bias from source functions, meteorological drivers, and aerosol processing. Modeled SSAer AOD compares well with satellite data, potentially indicating that improvements could be made to the size distributions to overcome the discrepancy in concentrations, assuming that the hygroscopicity factor is adequately represented.

*What are the implications of model diversity and changes in SSAer emissions, for the present and future polar climate?* Pre-industrial and future climate CMIP6 experiments show that models agree that a doubling of SSAer emissions exerts a net negative radiative perturbation at the top of the atmosphere in summer in the Arctic and the Antarctic, with less agreement for the sign of the impact in winter. In terms of surface temperature, models agree on a cooling effect in summer in the Arctic but disagree on the sign of the change for winter and for the Antarctic. These impacts are generally heterogeneous in terms of their spatial distribution, but the large uncertainty in the present-day emissions shown here means possibly an uncertainty of up to  $2 \text{ W m}^{-2}$  in the polar radiative budget. A multiplication of SSAer mass emissions in the Arctic by more than 2 in SSP585 (as indicated by the CMIP6 ensemble mean) could imply a regionally negative radiative impact around  $-1 \text{ W m}^{-2}$  in winter at the end of the century.

These conclusions highlight the need for additional research on the representation of SSAer at the poles. In particular, polar-specific source functions and size distribution could help improve the simulated concentrations according to our findings.

More complex and up-to-date parameterizations for SSAer emissions exist in the literature, including polar specific processes (sources from blowing snow, specific flux from leads... ). It would be interesting to test these parameterizations in global models, using appropriate size distributions. More than the mass, the number concentration by size needs to be validated when it comes to integrating aerosol-cloud interactions. Making

995 such outputs available in future CMIP experiments could thus be useful. Also, the or-  
996 ganic fraction and hygroscopic properties of SSaer will highly influence their radiative  
997 effect. Therefore, global models should work on including a realistic organic fraction for  
998 polar SSaer, and adapting hygroscopicity for the high latitudes. However, improving model  
999 performance for polar SSaer also requires more observations, particularly from blowing  
1000 snow and lead generated SSaer which still have large uncertainties. A joint effort between  
1001 observers, regional and global modelers is required in the future to address these issues.  
1002 Additionally, this work shows that aerosol-radiation and aerosol-cloud interactions of SSaer  
1003 at the poles cannot be ignored in models and need to be activated and accurately rep-  
1004 resented to obtain a reliable radiative budget, including to quantify anthropogenic aerosol  
1005 radiative effects.

## 1006 Open Research

1007 The scripts used for computations and figure creation, along with the observation  
1008 data used for model evaluation, can be found at the following repository: [https://doi](https://doi.org/10.5281/zenodo.7590005)  
1009 [.org/10.5281/zenodo.7590005](https://doi.org/10.5281/zenodo.7590005) (Lapere, 2023a). The MODIS-based sea aerosol opti-  
1010 cal depth product created for this work is available at: [https://doi.org/10.5281/zenodo](https://doi.org/10.5281/zenodo.7584063)  
1011 [.7584063](https://doi.org/10.5281/zenodo.7584063) (Lapere, 2023b).

## 1012 Author contributions

1013 RL: Conceptualization, Methodology, Formal analysis, Investigation, Writing - Orig-  
1014 inal Draft, Visualization. JT: Conceptualization, Methodology, Supervision, Writing -  
1015 Original Draft. LM: Conceptualization, Methodology, Supervision, Writing - Review &  
1016 Editing. MF, ML, BS, LS, XY, AE, RM, AR, MES, MS, PZ: Methodology, Writing -  
1017 Review & Editing.

## 1018 Acknowledgments

1019 This project has received funding from the European Union's Horizon 2020 research and  
1020 innovation programme under grant agreement No 101003826 via project CRiceS (Cli-  
1021 mate Relevant interactions and feedbacks: the key role of sea ice and Snow in the po-  
1022 lar and global climate system). The authors also acknowledge the EU H2020 FORCeS  
1023 project, contract No 821205. We also appreciate the effort of the CMIP6 modelling groups  
1024 which contributed the data to the CMIP6 data archive. We acknowledge Yves Balka-  
1025 nski, Jean-Christophe Raut and Dirk Olivié for the fruitful discussions. Furthermore,  
1026 the authors acknowledge EBAS/NILU for making the observation data available through  
1027 their platform. We also want to acknowledge the people responsible for these difficult  
1028 measurements that we downloaded from EBAS: Karin Sjoberg from the Swedish Envi-  
1029 ronmental Research Institute for the Bredkalen station, Arni Sigurdsson for the Irafoss  
1030 station, Wenche Aas from the Norwegian Institute for Air Research for the Karasjok and  
1031 Zeppelin stations, Timo Salmi from the Finnish Meteorological Institute for the Pallas  
1032 station, and Kaare Kemp from the National Environmental Research Institute, Denmark,  
1033 for the Villum station.

## Tables

**Table 1.** CMIP6 models considered and their sea spray source function and emission drivers. MA06 is (Mahowald et al., 2006), MO86 is (Monahan et al., 1986), MA03 is (Mårtensson et al., 2003), JA11 is (Jaeglé et al., 2011), GR14 is (Grythe et al., 2014), GO03 is (Gong, 2003), SA15 is (Salter et al., 2015), and SM98 is (M. H. Smith & Harrison, 1998). For the limit radii of sea salt aerosols, values in italic indicate smallest/largest lognormal modes instead of cut-off sizes.

Model	Source function	Drivers	Limit radii ( $\mu\text{m}$ )	Data used								
				<i>mmrss</i>	<i>siconc</i>	<i>sfcWind</i>	<i>emiss</i>	<i>od550ss</i>	<i>bldep</i>	<i>dryss/wetss</i>	<i>piClim</i>	<i>SSP</i>
BCC-ESM	MA06	Wind	0.1-10				x					
CESM	MO86, MA03	Wind, SST	0.02-10				x		x			
CNRM-ESM	JA11, GR14	Wind, SST	0.03-20						x			
EC-Earth	GO03, SA15	Wind, SST	<i>0.09-0.794</i>				x	x	x			
GISS	MO86	Wind	0.1-4				x		x			x
HadGEM	GO03	Wind	0.05-5				x		x			x
IPSL-CM6A	MO86, SM98	Wind	<i>0.1-1.185</i>				x	x	x		x	
MIROC-ES2L	MO86	Wind	0.1-10				x		x			x
MPI-ESM	MO86, SM98	Wind	<i>0.5</i>				x	x	x			
MRI-ESM	MO86	Wind	<i>0.13-1.75</i>				x	x				x
NorESM	SA15	Wind, SST	<i>0.0475-0.75</i>				x	x	x		x	x
UKESM	GO03	Wind	0.05-5				x		x		x	x

## Full model names and CMIP6 references

- The Beijing Climate Center Earth System Model (Wu et al., 2020) – BCC-ESM1
- The Community Earth System Model (Danabasoglu et al., 2020) – CESM2
- The Centre National de Recherches Météorologiques Earth System Model (Séférian et al., 2019) – CNRM-ESM2-1
- The European Community Earth System Model (Döscher et al., 2022) – EC-Earth3-AerChem
- The NASA Goddard Institute for Space Studies Earth System Model (Miller et al., 2021) – GISS-E2-1-H
- The Hadley Centre Global Environmental Model (Sellar et al., 2020) – HadGEM3-GC31-LL
- The Institut Pierre Simon Laplace Climate Model (Boucher et al., 2020) – IPSL-CM6A-LR-INCA
- The Model for Interdisciplinary Research on Climate Earth System for Long-term simulations (Hajima et al., 2020) – MIROC-ES2L
- The Max Planck Institute Earth System Model (Gutjahr et al., 2019) – MPI-ESM-1-2-HAM
- The Meteorological Research Institute Earth System Model (Yukimoto et al., 2019) – MRI-ESM2-0
- The Norwegian Earth System Model (Seland et al., 2020) – NorESM2-LM
- The UK Earth System Model (Sellar et al., 2020) – UKESM1-0-LL

**Table 2.** Regionally averaged mean change in top-of-the-atmosphere net downward radiation between the *piClim-2xss* and *piClim-control* scenario.  $\pm$  indicate 95% confidence intervals. Bold values indicate that the radiative impact is significant at the 95% level according to a Wilcoxon test. Arctic is all grid points north of 60°N and Antarctic is all grid points south of 60°S.

	Arctic		Antarctic	
	Dec–Feb	Jun–Aug	Jun–Aug	Dec–Feb
IPSL-CM6	<b>0.17±0.01</b>	<b>-0.48±0.03</b>	0.01±0.008	<b>-0.34±0.02</b>
NorESM	<b>-0.61±0.01</b>	<b>-0.29±0.04</b>	<b>-0.12±0.01</b>	<b>-1.01±0.07</b>
UKESM	<b>-0.33±0.01</b>	<b>-0.24±0.01</b>	<b>0.09±0.005</b>	<b>-0.37±0.02</b>



## Figures

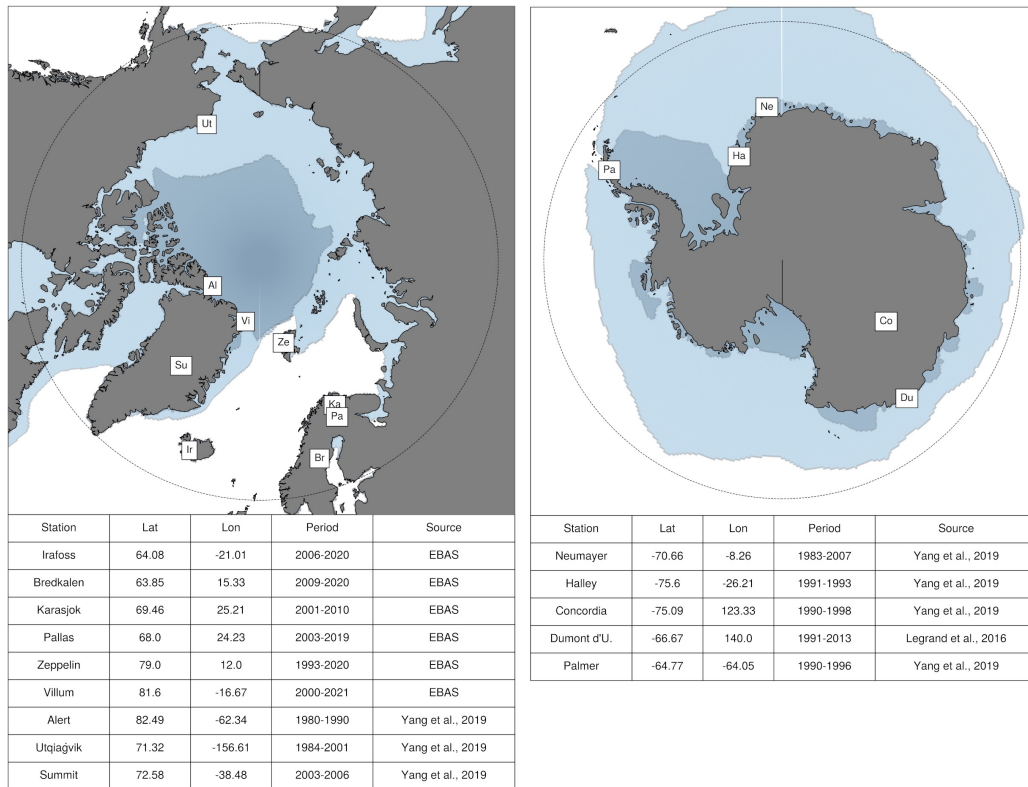


**Figure 1.** Arctic and Antarctic measurement stations providing sea salt surface mass concentration data. Blue colormaps indicate areas with a sea ice concentration above 50%. The lighter blue is for February in the Arctic, and August in the Antarctic. The darker blue is the opposite. The sea ice data are from ERA5. The black dashed line shows the 60° limit considered for regional aggregated analyses. Abbreviations in the maps are the first two letters of the corresponding station name.

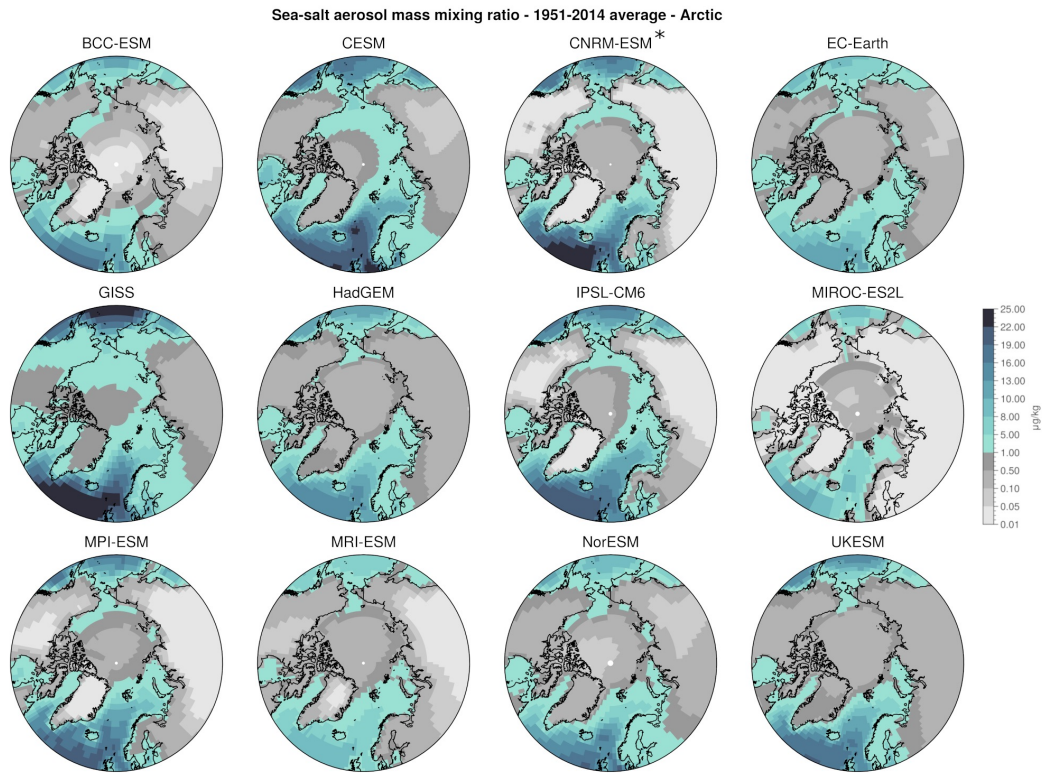
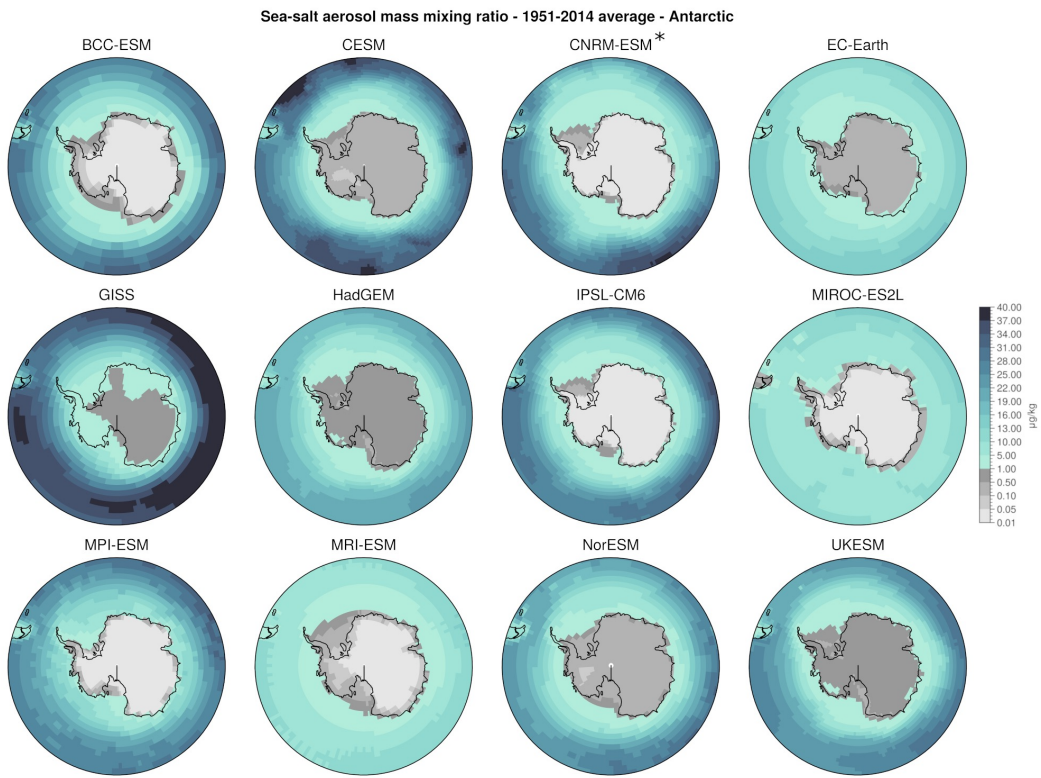


**Figure 2.** Sea salt aerosol mass mixing ratio in the lowest model level. Annual average for the period 1951–2014 in the CMIP6 historical scenario. Arctic map. NB: CNRM-ESM values are divided by 25 to fit in the colorbar.



	>60N						<60S						Global
BCC-ESM		11	207	4				43	224	13			
CESM	88	27	956		28	54	187	57	943		63	121	55
CNRM-ESM	3922	500	289	5			6973	1020	425	7			6
EC-Earth	120	14	515	6	99	30	272	35	655	17	220	59	14
GISS	53	31	299	90	12	54	135	109	314	201	31	132	29
HadGEM	82	15	581				201	42	667				18
IPSL-CM6	186	23	138	11	177	25	304	46	116	12	286	28	7
MIROC-ES2L	72	7	205		22	35	309	40	223		83	122	6
MPI-ESM	131	20	202	6	26	86	424	75	203	15	95	245	19
MRI-ESM	79	10	168	11	53	34	124	21	189	15	90	46	8
NorESM	64	14	479	15	26	39	161	44	566	29	58	83	34
UKESM	100	16	573				249	47	656				14
	Mass emissions (Tg/yr)	Mass mixing ratio ( $\times 10^{-6}$ g/g)	Aerosol layer height (m)	AOD ( $\times 1000$ )	Dry deposition (Tg/year)	Wet deposition (Tg/year)	Mass emissions (Tg/yr)	Mass mixing ratio ( $\times 10^{-6}$ g/g)	Aerosol layer height (m)	AOD ( $\times 1000$ )	Dry deposition (Tg/year)	Wet deposition (Tg/year)	Lifetime (hour)

**Figure 4.** Model diversity in mass emissions, surface mass mixing ratio, aerosol layer height, AOD, dry and wet deposition, and lifetime of sea salt aerosol. Average for the period 1951–2014. The color scale highlights the highest values for each column. CNRM-ESM is excluded from this color scale for mass emission and *mmrss*. Empty cells indicate that values are not provided by the model. *mmrss* is multiplied by 10 and AOD is multiplied by 1000 for improved readability.

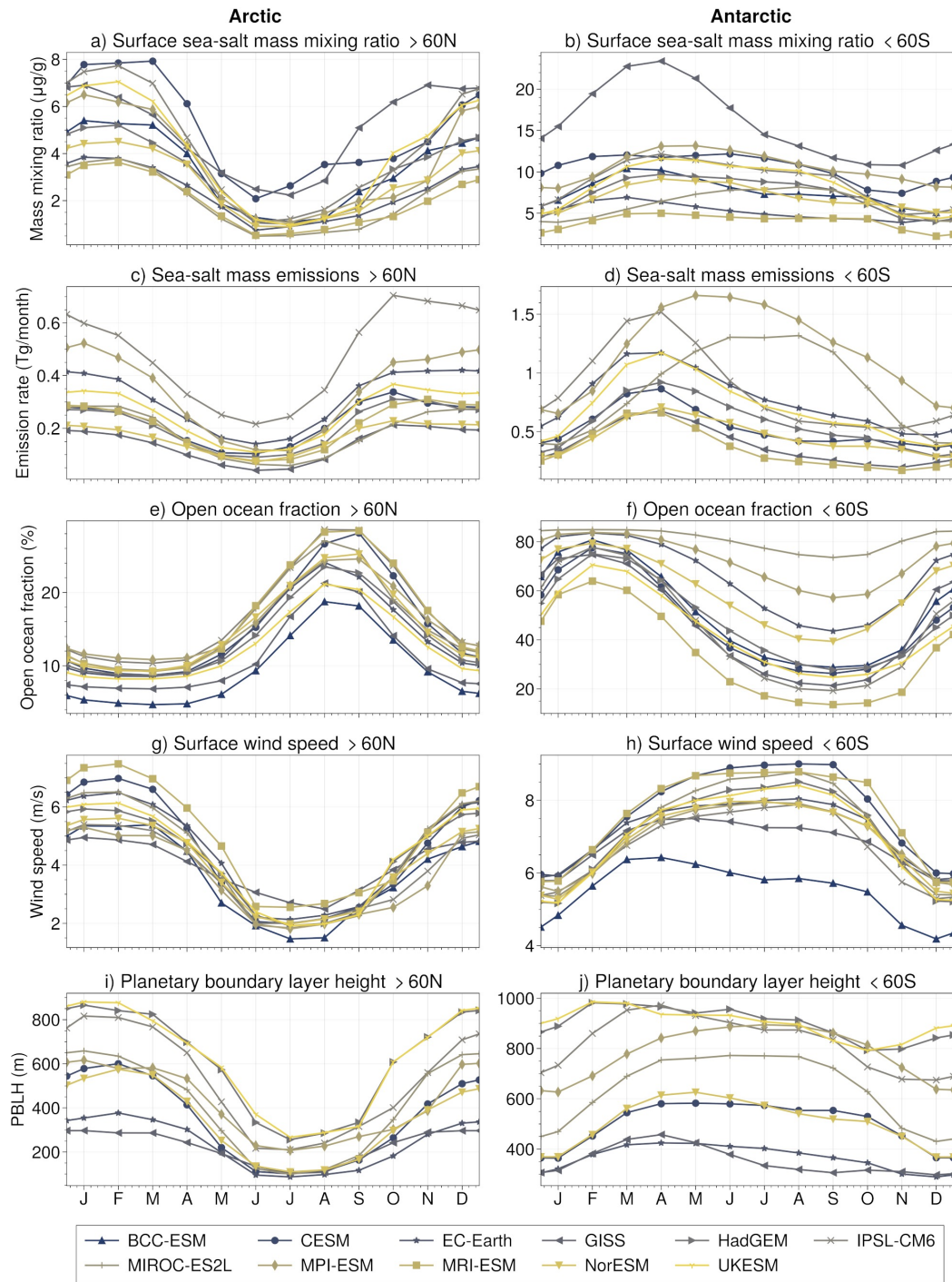


**Figure 5.** Annual cycles of sea salt aerosol mass mixing ratio at surface level (a,b), sea salt aerosol mass emission (c,d), fraction of open ocean (e,f), surface wind speed (g,h) and planetary boundary layer height (i,j) at latitudes above  $60^{\circ}\text{N}$  (left) and below  $60^{\circ}\text{S}$  (right) in CMIP6 models for the period 1951–2014. Lines show the monthly average over the period for each model. Emissions are summed to obtain the total emission flux over the considered region. Mixing ratio, wind speed and planetary boundary layer height are averaged for grid points over the ocean, with non-zero emissions and less than 90% sea ice cover. The open ocean fraction is computed as one minus the average of the sea ice concentration over the considered region. Panels (i,j) only include the 9 models providing the *bldep* variables (i.e. all except BCC-ESM, CNRM-ESM and MRI-ESM). Panels (c,d) do not include BCC-ESM as emission rates are not available for that model. CNRM-ESM is not included in this analysis.

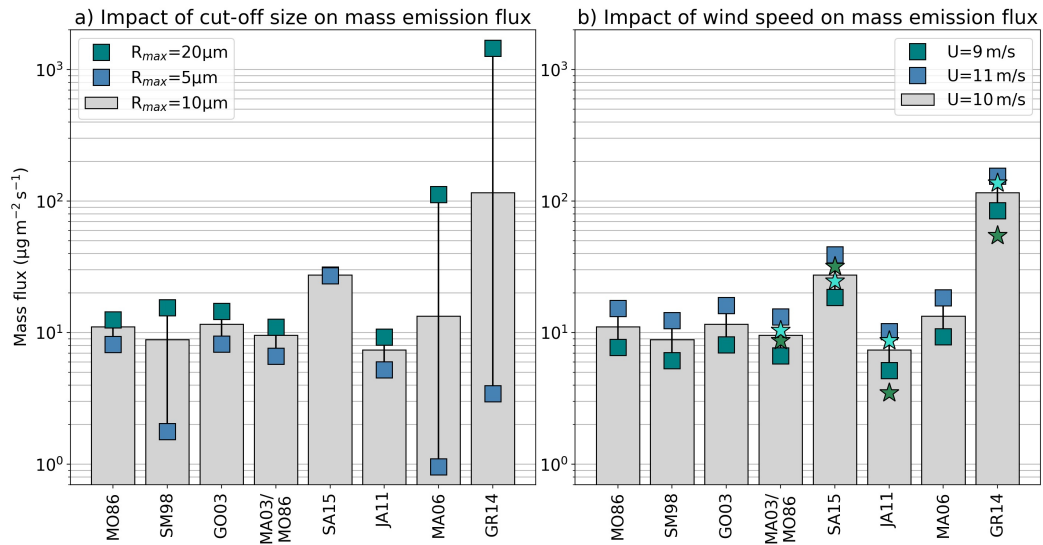


**Figure 6.** Sea salt aerosol source functions used in CMIP6 models. a) effect on the mass emission flux of changing the aerosol cut-off radius ( $R_{max}$ ), at  $10\text{ m s}^{-1}$  wind speed and  $5^\circ\text{C}$  SST. b) effect of changing wind speed ( $U$ ) on the mass emission flux for a cut-off radius at  $10\text{ }\mu\text{m}$ . Green and blue stars indicate mass emission fluxes for  $0$  and  $10^\circ\text{C}$  SST, respectively, at  $10\text{ m s}^{-1}$  wind speed. In both panels, size bin limits are taken as  $0.05\text{-}0.5\text{-}1\text{-}R_{max}\text{ }\mu\text{m}$ .

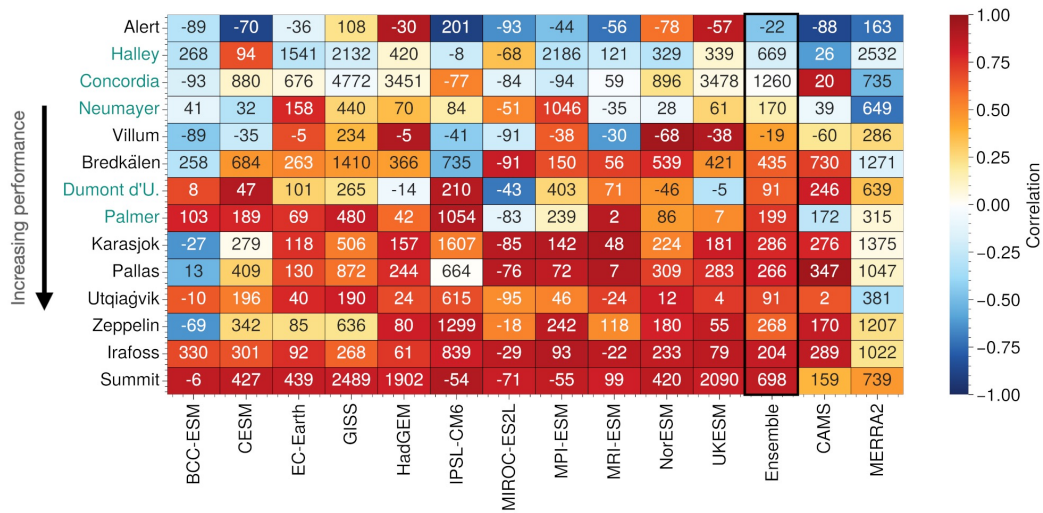


**Figure 7.** Normalized mean bias (numbers, in percent) and Pearson correlation coefficient (colormap) with respect to 9 stations in the Arctic (in black) and 5 stations in the Antarctic (in blue). CMIP6 individual models and ensemble mean are for the period 1951–2014, CAMS reanalysis is for 2003–2021 and MERRA2 is for 1980–2021. See Figures 8 and A2 for individual comparisons of time series.

Accepted Article

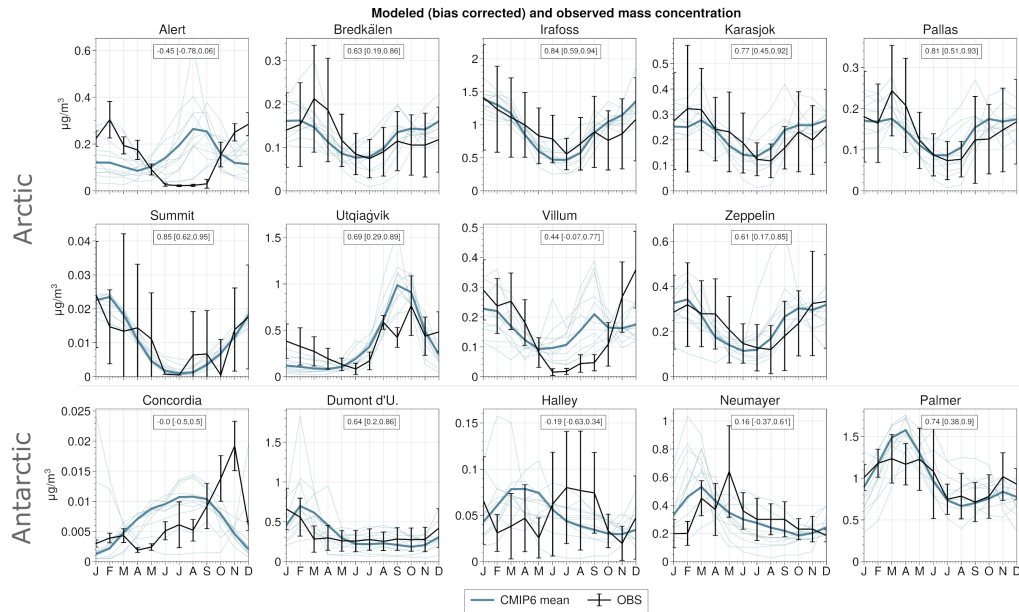


**Figure 8.** Annual cycle of sodium aerosol surface mass concentrations at 9 stations in the Arctic (top and middle) and 5 stations in the Antarctic (bottom). Observations are in black (caps show one standard deviation of monthly means), individual CMIP6 models (1951–2014) are in light blue, CMIP6 ensemble mean (solid thick line) is in blue. CMIP6 values are bias corrected by applying a factor  $\langle \text{OBS} \rangle / \langle \text{MODEL} \rangle$ . Boxes indicate the Pearson correlation coefficient between the annual cycle in CMIP6 ensemble mean and observations, with the 95% confidence interval between brackets.



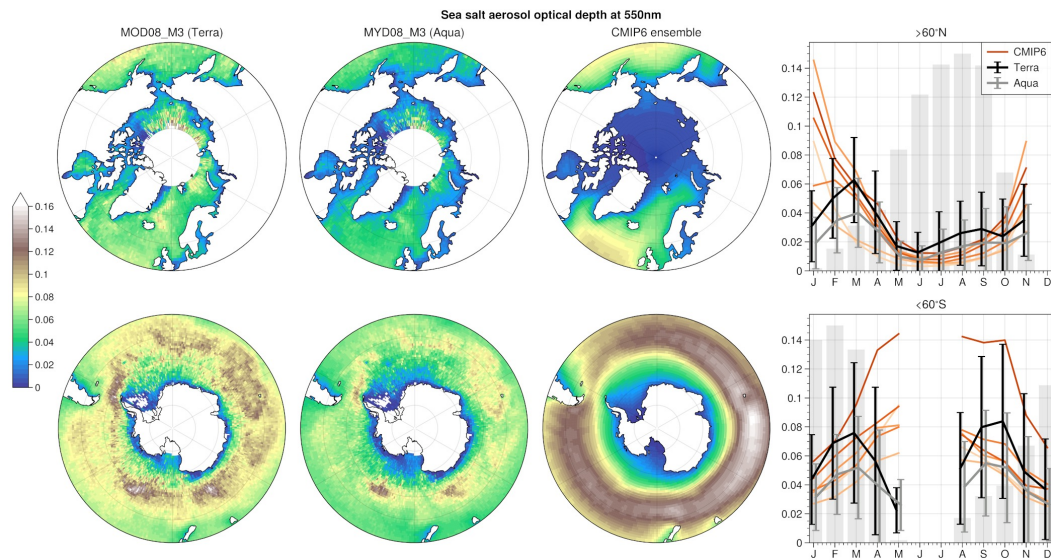


**Figure 9.** CMIP6 ensemble median and MODIS Terra (MOD08.M3) and Aqua (MYD08.M3) Dark Target/Deep Blue sea salt aerosol optical depth at 550 nm. Both MODIS data sets and CMIP6 model data are averages of monthly means for the period 2005–2014. The CMIP6 ensemble contains a subset of models providing the *od550ss* variable (BCC-ESM, EC-Earth, IPSL-CM6, MPI-ESM, MRI-ESM, NorESM). MODIS values are adjusted to only account for the contribution to AOD of particles with Angstrom exponent below 1. Right: average annual cycles of sea salt aerosol optical depth in MODIS (Terra in black, Aqua in grey - caps show one standard deviation) and CMIP6 models (orange). MODIS and CMIP6 values are collocated, i.e. CMIP6 values are used only for those grid cells where MODIS has valid records. Gray bars indicate, on an arbitrary scale common to both panels, the number of available records in MODIS Terra.

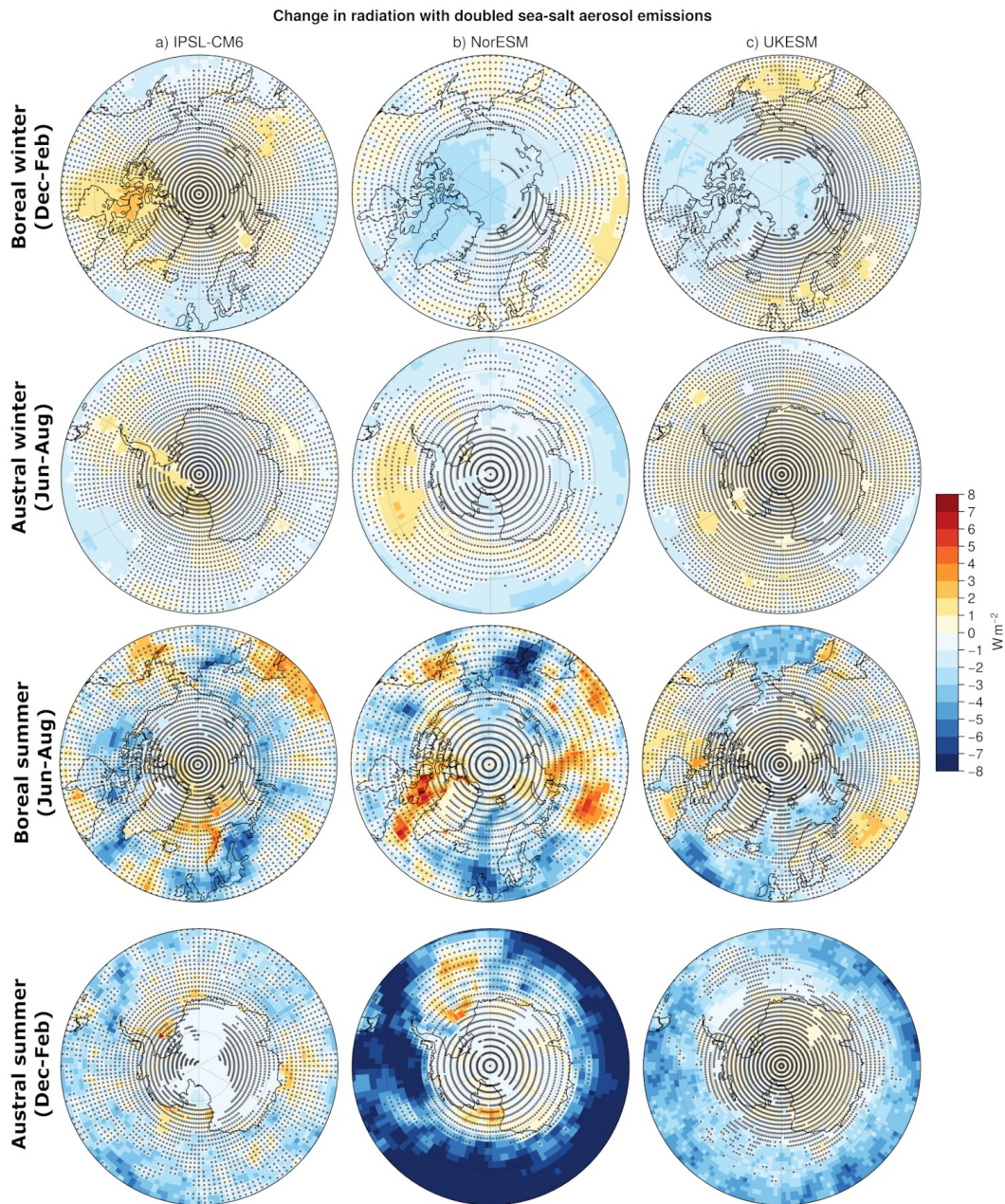


**Figure 10.** Change in top-of-the-atmosphere net downward radiative flux ( $rtmt$ ) in a scenario with doubled sea salt aerosol emissions under pre-industrial atmospheric composition (30 years under 1850 conditions). Stippling shows the grid points for which the difference between *piClim-2xss* and *piClim-control* is not significant at the 90% level according to a Wilcoxon test.

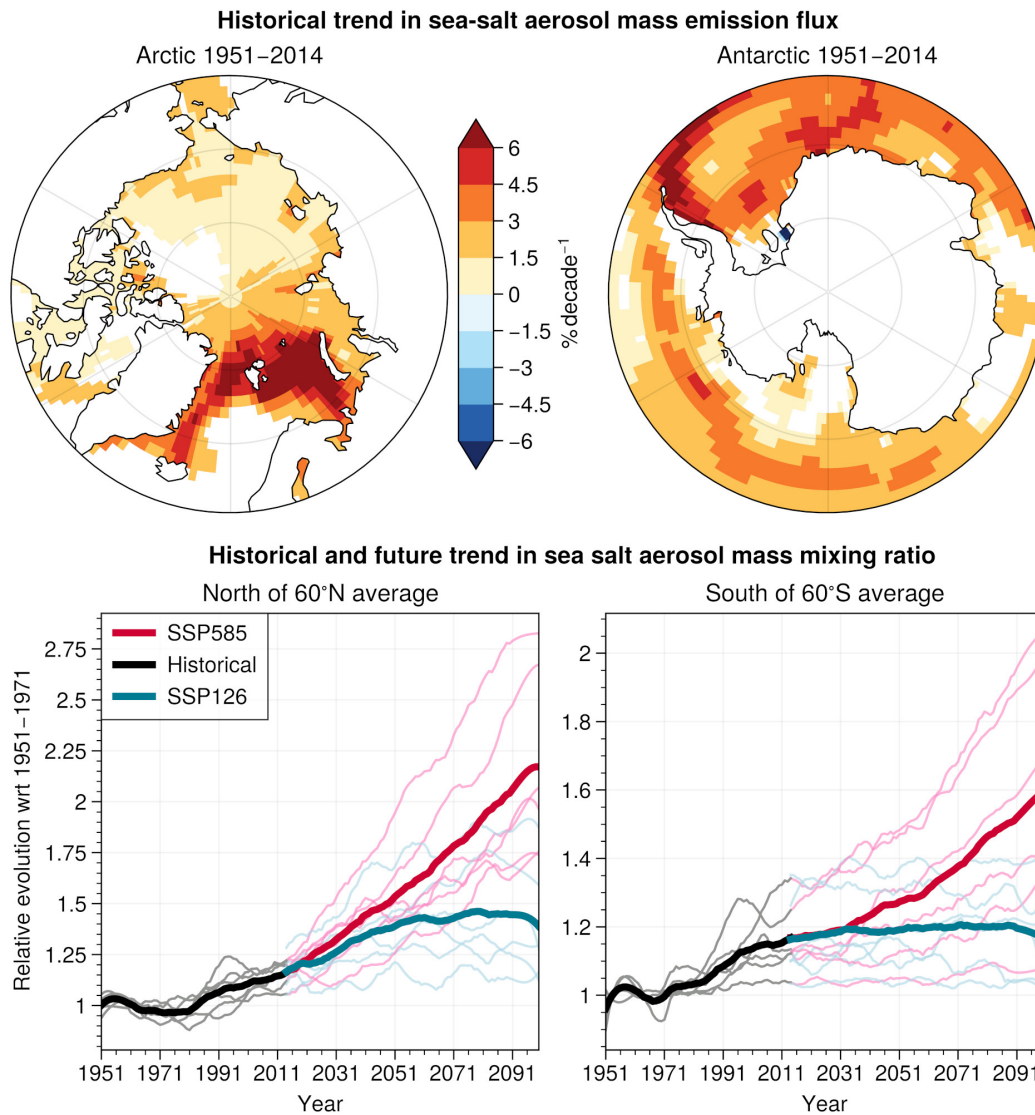


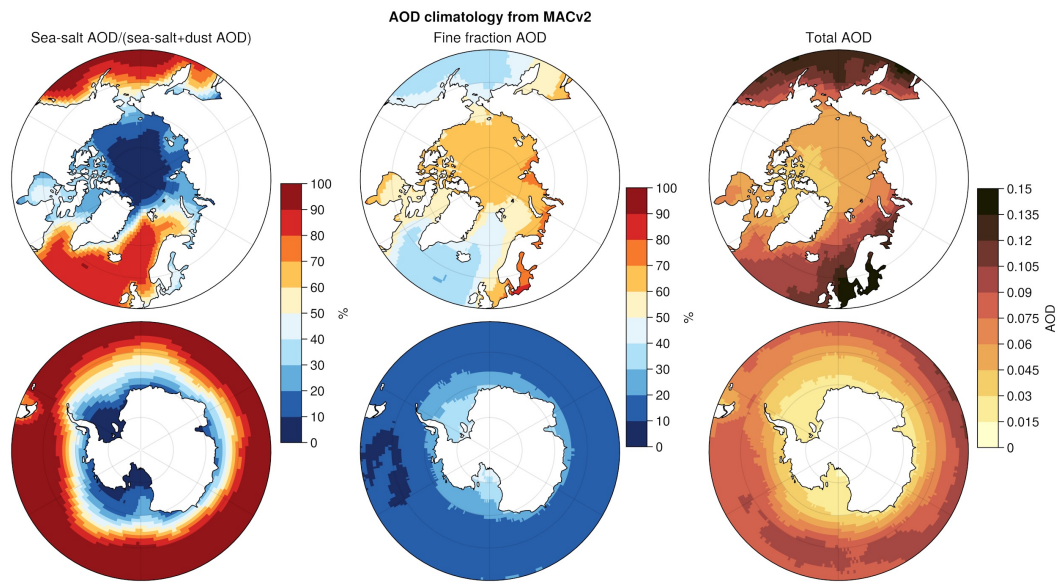
**Figure 11.** Top: trends in sea salt aerosol mass emissions in the ensemble mean for the period 1951–2014. The mass emission is normalized by the 1951–2014 average to obtain %/decade. Bottom: historical and future (relative to the 1951–1971 mean) yearly time series (1951–2099) of average sea salt surface mass mixing ratio north of 60°N (left) and south of 60°S (right), including ocean and land. Mixing ratios are weighted by grid cell area for spatial averaging. Time series are smoothed using a Savitzky-Golay filter with a window length of 19 years and a polynomial order 3. Ensemble means are shown as thicker lines (black for the historical period, blue for SSP126, red for SSP585). Individual members use the same color code but with thinner lines. Included models are: GISS, HadGEM, MIROC-ES2L, MRI-ESM, NorESM and UKESM. The smallest (largest, respectively) trend in SSP585 corresponds to NorESM (UKESM, respectively).

**Appendix A**

**Table A1.** Regionally averaged mean change in surface temperature (*tas* variable - °C) in the CMIP6 ensemble of models GISS, HadGEM, MIROC-ES2L, MRI-ESM, NorESM and UKESM. This change is computed as the difference between the 2000–2014 historical and 2085–2100 future averages. Arctic is all grid points north of 60°N, Antarctic is all grid points south of 60°S. Spread here refers to the difference between the model with largest increase and the model with smallest increase.

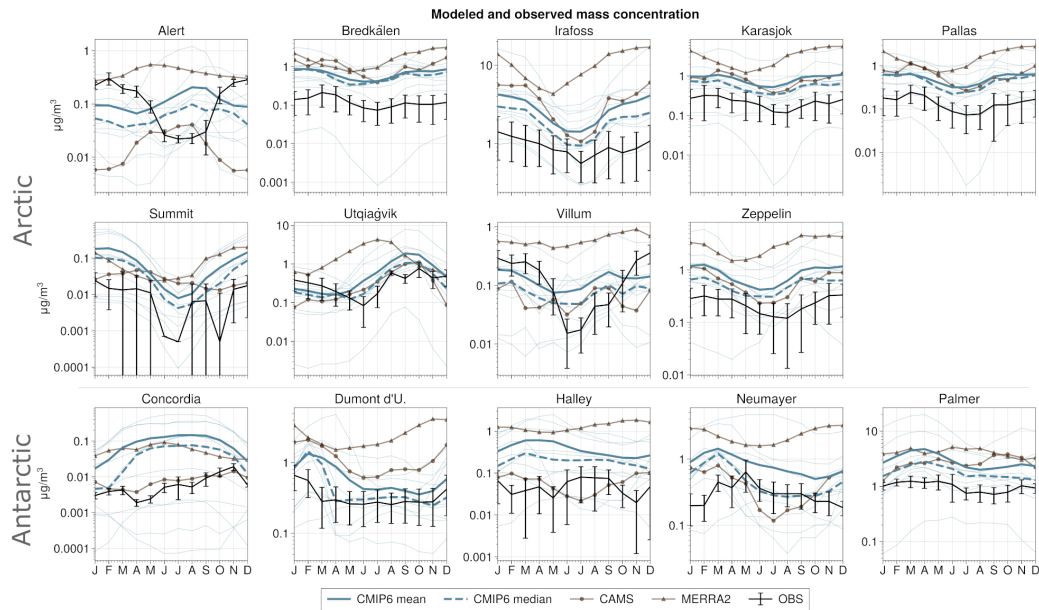
	Global		Arctic		Antarctic	
	Mean	Spread	Mean	Spread	Mean	Spread
SSP126	1.5	2.0	3.8	7.4	1.0	1.5
SSP585	5.1	3.8	10.8	10.0	4.5	3.1

## A1 Sea salt dominance assessed from MACv2

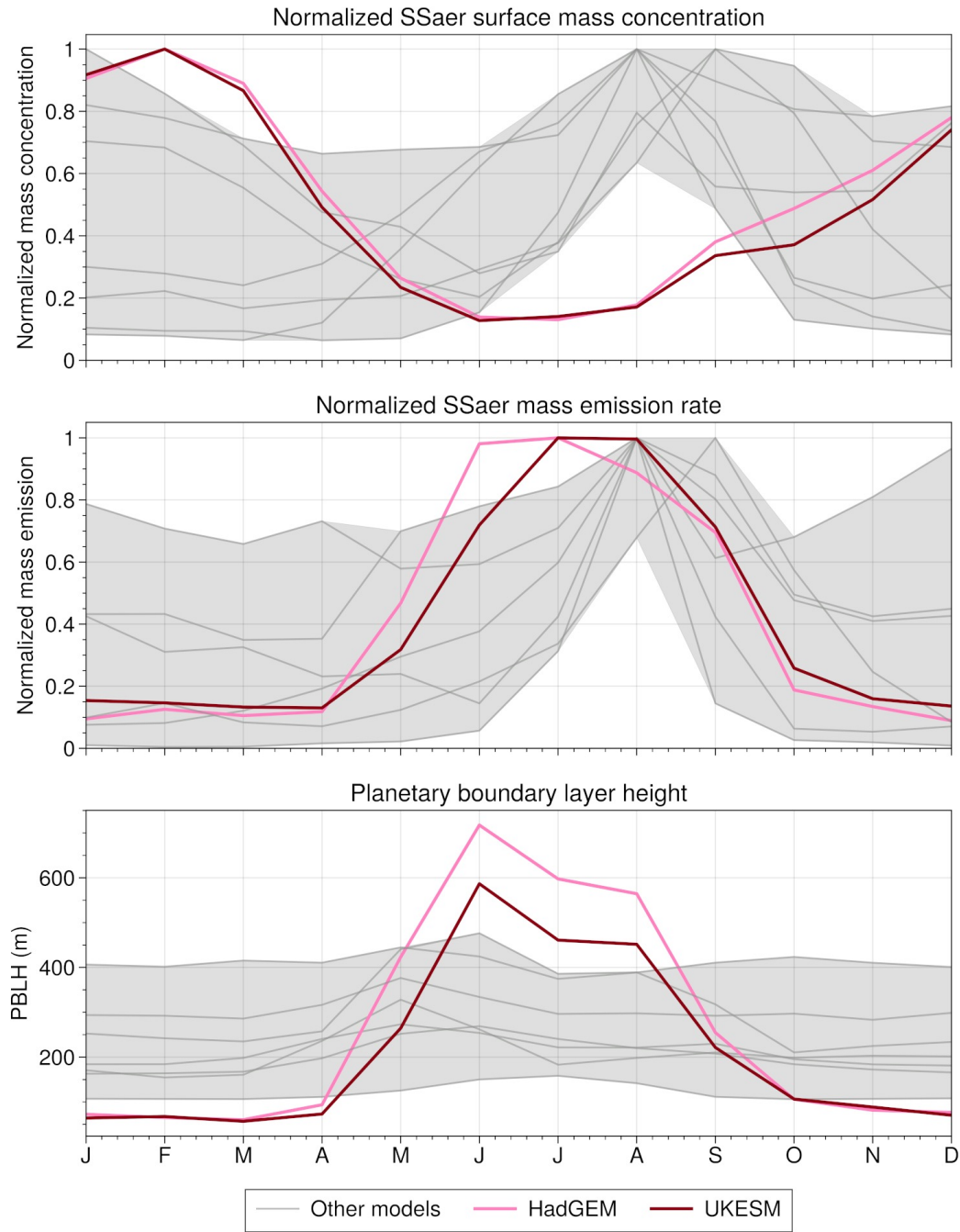


**Figure A1.** AOD characteristics at the poles from the MACv2 climatology (Kinne, 2019). Left: fraction of coarse AOD (dust+sea salt) attributed to sea salt (annual average climatology). Only dust and sea salt are considered here since we look at the coarse fraction AOD. Middle: fraction of total AOD from fine mode aerosols. Right: total AOD.

## A2 Non-normalized annual cycles versus observations



**Figure A2.** Annual cycle of sodium aerosol surface mass concentrations at 9 stations in the Arctic (top and middle) and 5 stations in the Antarctic (bottom). Observations are in black (caps show one standard deviation of monthly means), individual CMIP6 models (1951–2014) are in light blue, CMIP6 ensemble mean (solid line) and median (dashed line) is in darker blue, reanalyses (CAMS 2003–2021 - circles - and MERRA2 1980–2021 - triangles) are in brown.

**A3 Annual cycles at Alert**

**Figure A3.** Annual cycles of SSAer mass concentration (top - normalized), SSAer mass emission (middle - normalized) and boundary layer height (bottom) in CMIP6 at the grid point nearest to the Alert station. Average annual cycles for the period 1951–2014.

1040

**A4 Vertical distribution of SSaer and clouds**

1041

1042

1043

1044

1045

1046

1047

1048

1049

The evaluation conducted in Section 3.1 mainly focused on surface and column-integrated SSaer variables. To connect SSaer to clouds, information on the vertical distribution is needed. Figure A4 shows the regionally averaged profiles of *mrrss* in the Arctic and Antarctic in the historical period, in Jun–Aug and Dec–Feb. This figure shows that the diversity at the surface affects also the vertical distribution. The inter-model spread is roughly constant from the surface up to 400 m altitude and remains above  $1 \mu\text{g g}^{-1}$  at 10 km altitude in winter months. Given that SSaer are injected high enough to interact with clouds (Figure A4), part of the diversity in cloud profiles at the poles could stem from this diversity in SSaer profile. In summer months, the profiles converge more rapidly.

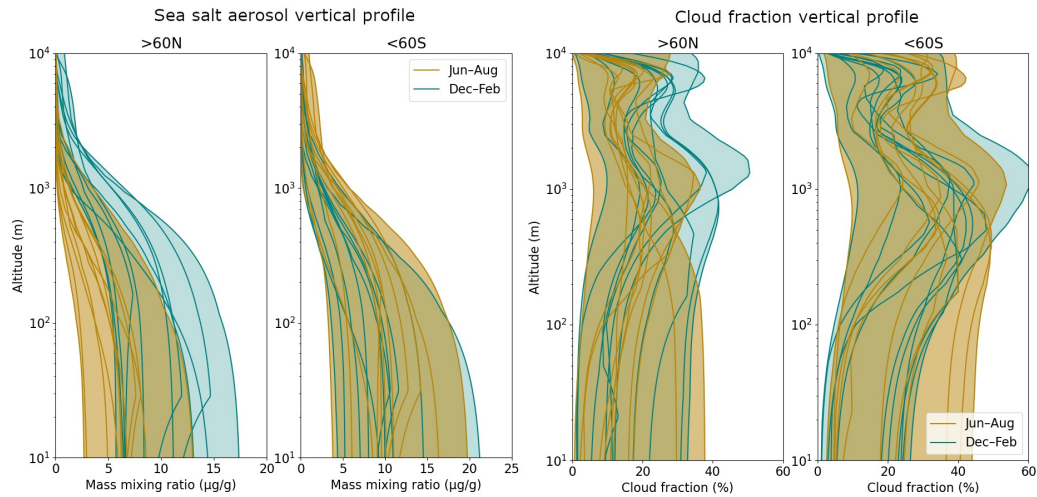


**Figure A4.** Left: Average vertical profile of sea salt aerosol mass mixing ratio in the Arctic (above  $60^\circ\text{N}$  - left) and Antarctic (below  $60^\circ\text{S}$  - right) in individual CMIP6 models, for Jun–Aug (blue) and Dec–Feb (yellow). Each line corresponds to one model, and the shaded area marks the ensemble envelope. Only grid points with less than 50% sea ice concentration are considered in this figure. Right: same as left but for cloud fraction. NB: the vertical axis is in logarithmic scale.



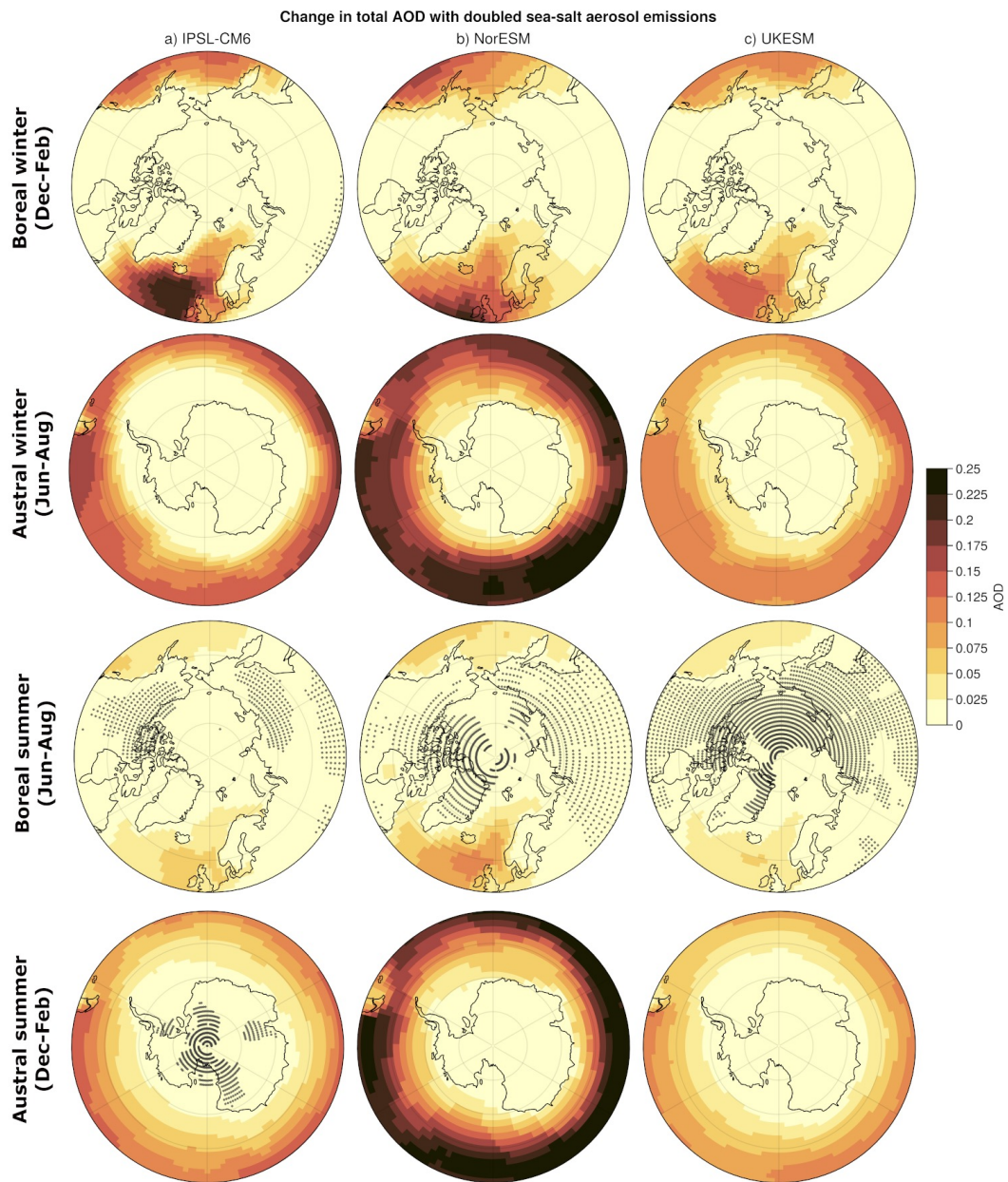
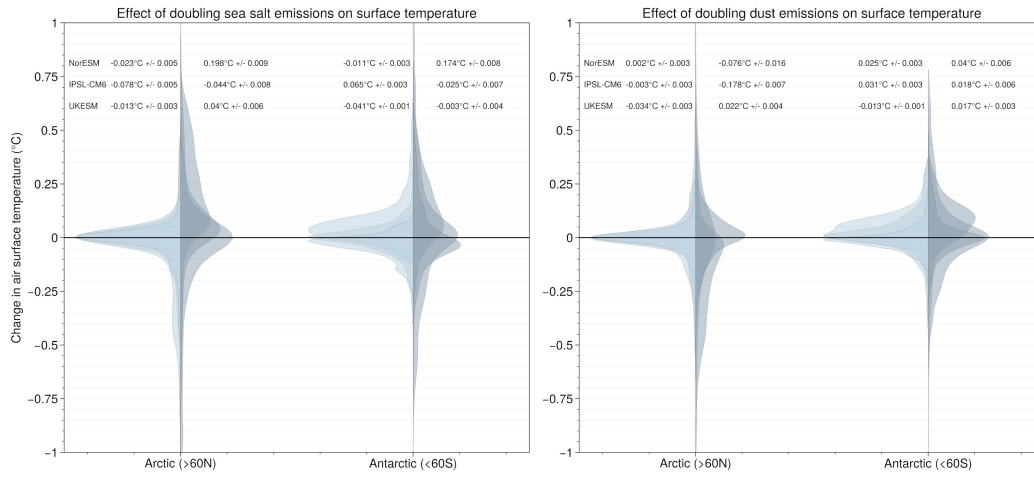
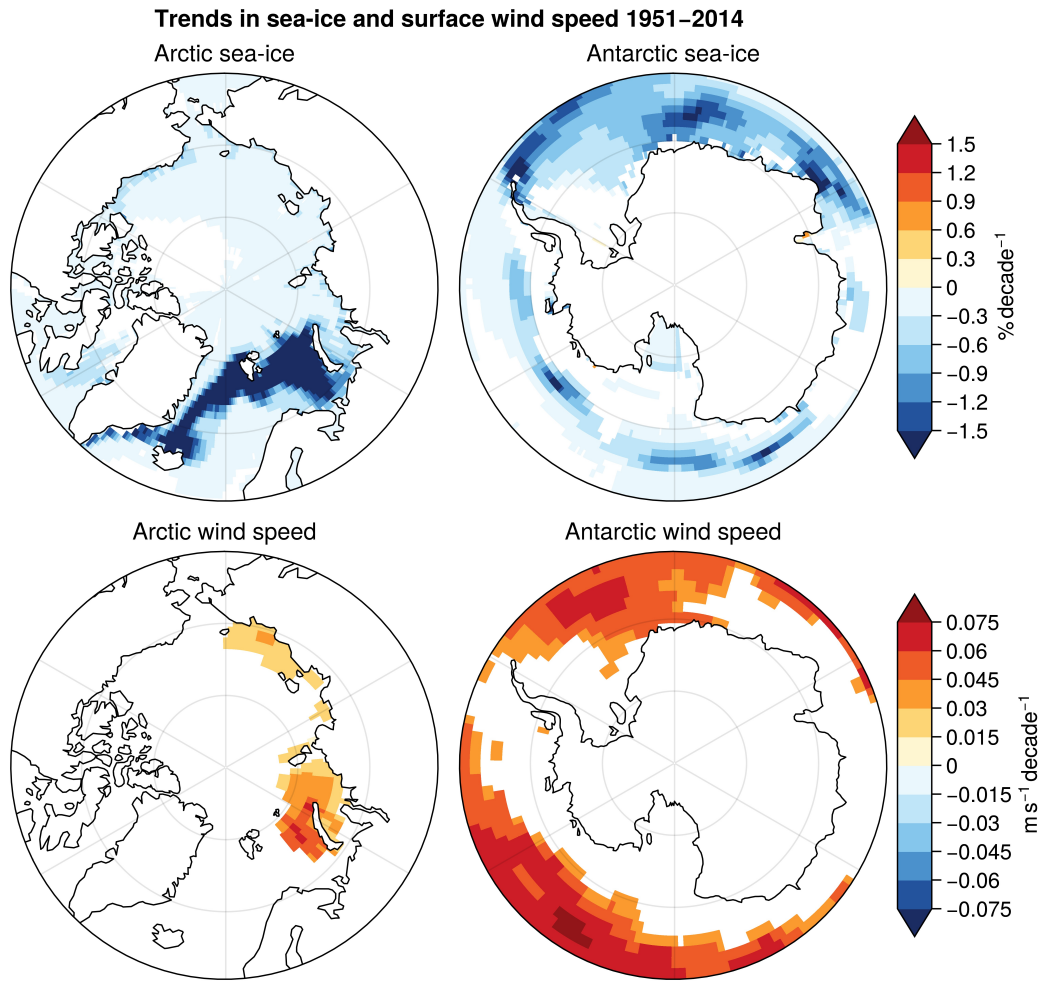
A5 *piClim-2xss* scenario

Figure A5. Same as Figure 10 but for total aerosol optical depth ( $od550aer$ ).



**Figure A6.** Difference in air surface temperature in the *piClim-control* and the *piClim-2xss* (left) and *piClim-2xdust* (right) experiments. Models included: IPSL-CM6, NorESM and UKESM. Summer is Jun–Aug in the Arctic, Dec–Feb in the Antarctic, and vice-versa. Values along the x-axis indicate the normalized frequency of temperature changes.

## A6 Drivers of sea salt emission trends



**Figure A7.** Historical trends in sea ice concentration (top) and surface wind speed (bottom) in CMIP6 models for the period 1951–2014. Included models are: GISS, HadGEM, MIROC-ES2L, MRI-ESM, NorESM and UKESM. Trends are computed following Mann-Kendall’s test. Only significant trends at the 95% level are shown.

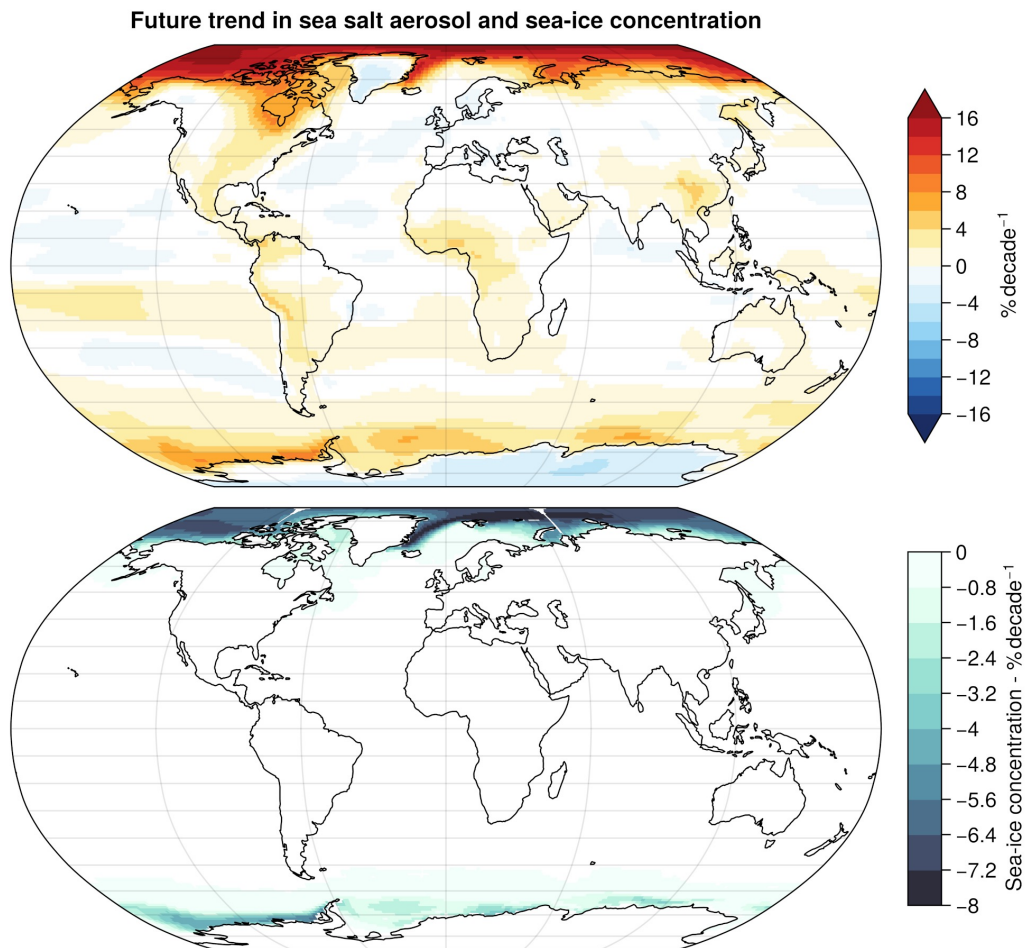


**Figure A8.** Maps of future trends in annual mean sea salt aerosol surface mass mixing ratio (top) and sea-ice concentration (bottom). Scenario SSP585. Multi-model mean from GISS, HadGEM, MIROC-ES2L, MRI-ESM, NorESM and UKESM.

## References

- Alkama, R., Taylor, P. C., Garcia-San Martin, L., Douville, H., Duveiller, G., Forzieri, G., . . . Cescatti, A. (2020). Clouds damp the radiative impacts of polar sea ice loss. *The Cryosphere*, *14*, 2673–2686. doi: 10.5194/tc-14-2673-2020
- Allen, R. J., & Sherwood, S. C. (2011). The impact of natural versus anthropogenic aerosols on atmospheric circulation in the Community Atmosphere Model. *Climate Dynamics*, *36*, 1959–1978. doi: 10.1007/s00382-010-0898-8
- Andreae, M. O., & Rosenfeld, D. (2008). Aerosol–cloud–precipitation interactions. Part 1. The nature and sources of cloud-active aerosols. *Earth-Science Reviews*, *89*, 13–41. doi: 10.1016/j.earscirev.2008.03.001
- Atmoko, D., & Lin, T.-H. (2022). Sea Salt Aerosol Identification Based on Multispectral Optical Properties and Its Impact on Radiative Forcing over the Ocean. *Remote Sensing*, *14*, 3188. doi: 10.3390/rs14133188
- Bian, H., Froyd, K., Murphy, D. M., Dibb, J., Darnenov, A., Chin, M., . . . Smirnov, A. (2019). Observationally constrained analysis of sea salt aerosol in the marine atmosphere. *Atmospheric Chemistry and Physics*, *19*, 10773–10785. doi: 10.5194/acp-19-10773-2019
- Boucher, O., Randall, D., Artaxo, P., Bretherton, C., Feingold, G., Forster, P., . . . Zhang, X. Y. (2013). Climate Change 2013: The Physical Science Basis. Contribution of Working Group I to the Fifth Assessment Report of the Intergovernmental Panel on Climate Change [Stocker, T.F., D. Qin, G.-K. Plattner, M. Tignor, S.K. Allen, J. Boschung, A. Nauels, Y. Xia, V. Bex and P.M. Midgley (eds.)]. In (pp. 571–657). Cambridge University Press, Cambridge, UK and New York, NY, USA. doi: 10.1017/CBO9781107415324.016
- Boucher, O., Servonnat, J., Albright, A. L., Aumont, O., Balkanski, Y., Bastrikov, V., . . . Vuichard, N. (2020). Presentation and Evaluation of the IPSL-CM6A-LR Climate Model. *Journal of Advances in Modeling Earth Systems*, *12*, e2019MS002010. doi: 10.1029/2019MS002010
- Browse, J., Carslaw, K. S., Mann, G. W., Birch, C. E., Arnold, S. R., & Leck, C. (2014). The complex response of Arctic aerosol to sea-ice retreat. *Atmospheric Chemistry and Physics*, *14*, 7543–7557. doi: 10.5194/acp-14-7543-2014
- Burgos, M. A., Andrews, E., Titos, G., Benedetti, A., Bian, H., Buchard, V., . . . Zieger, P. (2020). A global model–measurement evaluation of particle light scattering coefficients at elevated relative humidity. *Atmospheric Chemistry and Physics*, *20*, 10231–10258. doi: 10.5194/acp-20-10231-2020
- Cai, Z., You, Q., Wu, F., Chen, H. W., Chen, D., & Cohen, J. (2021). Arctic Warming Revealed by Multiple CMIP6 Models: Evaluation of Historical Simulations and Quantification of Future Projection Uncertainties. *Journal of Climate*, *34*, 4871–4892. doi: 10.1175/JCLI-D-20-0791.1
- Chen, Y., Cheng, Y., Ma, N., Wei, C., Ran, L., Wolke, R., . . . Wiedensohler, A. (2020). Natural sea-salt emissions moderate the climate forcing of anthropogenic nitrate. *Atmospheric Chemistry and Physics*, *20*, 771–786. doi: 10.5194/acp-20-771-2020
- Curry, J. A., Schramm, J. L., Rossow, W. B., & Randall, D. (1996). Overview of Arctic Cloud and Radiation Characteristics. *Journal of Climate*, *9*, 1731–1764. doi: 10.1175/1520-0442(1996)009<1731:OOACAR>2.0.CO;2
- Dada, L., Angot, H., Beck, I., Baccarini, A., Quéléver, L. L. J., Boyer, M., . . . Schmale, J. (2022). A central arctic extreme aerosol event triggered by a warm air-mass intrusion. *Nature Communications*, *13*, 1–15. doi: 10.1038/s41467-022-32872-2
- Danabasoglu, G., Lamarque, J.-F., Bacmeister, J., Bailey, D. A., DuVivier, A. K., Edwards, J., . . . Strand, W. G. (2020). The Community Earth System Model Version 2 (CESM2). *Journal of Advances in Modeling Earth Systems*, *12*, e2019MS001916. doi: 10.1029/2019MS001916
- Dasarathy, S., Kar, J., Tackett, J., Rodier, S. D., Lu, X., Vaughan, M., . . . Bow-

- 1107 man, J. S. (2021). Multi-Year Seasonal Trends in Sea Ice, Chlorophyll Con-  
 1108 centration, and Marine Aerosol Optical Depth in the Bellingshausen Sea.  
 1109 *Journal of Geophysical Research: Atmospheres*, *126*, e2021JD034737. doi:  
 1110 10.1029/2021JD034737
- 1111 DeMott, P. J., Hill, T. C. J., McCluskey, C. S., Prather, K. A., Collins, D. B., Sul-  
 1112 livan, R. C., ... Franc, G. D. (2016). Sea spray aerosol as a unique source  
 1113 of ice nucleating particles. *Proc Natl Acad Sci U S A*, *113*, 5797–5803. doi:  
 1114 10.1073/pnas.1514034112
- 1115 Diaconescu, E. P., Mailhot, A., Brown, R., & Chaumont, D. (2018). Evalua-  
 1116 tion of CORDEX-Arctic daily precipitation and temperature-based climate  
 1117 indices over Canadian Arctic land areas. *Clim Dyn*, *50*, 2061–2085. doi:  
 1118 10.1007/s00382-017-3736-4
- 1119 Dror, T., Lehahn, Y., Altaratz, O., & Koren, I. (2018). Temporal-Scale Anal-  
 1120 ysis of Environmental Controls on Sea Spray Aerosol Production Over the  
 1121 South Pacific Gyre. *Geophysical Research Letters*, *45*, 8637–8646. doi:  
 1122 10.1029/2018GL078707
- 1123 Döscher, R., Acosta, M., Alessandri, A., Anthoni, P., Arsouze, T., Bergman, T., ...  
 1124 Zhang, Q. (2022). The EC-Earth3 Earth system model for the Coupled Model  
 1125 Intercomparison Project 6. *Geoscientific Model Development*, *15*, 2973–3020.  
 1126 doi: 10.5194/gmd-15-2973-2022
- 1127 Eastman, R., & Warren, S. G. (2010). Interannual Variations of Arctic Cloud  
 1128 Types in Relation to Sea Ice. *Journal of Climate*, *23*, 4216–4232. doi:  
 1129 10.1175/2010JCLI3492.1
- 1130 ESGF. (2014). The Earth System Grid Federation: An open infrastructure for ac-  
 1131 cess to distributed geospatial data. *Future Gener. Comput. Syst*, *36*, 400–417.  
 1132 doi: 10.1016/j.future.2013.07.002
- 1133 Fanourgakis, G. S., Kanakidou, M., Nenes, A., Bauer, S. E., Bergman, T., Carslaw,  
 1134 K. S., ... Yu, F. (2019). Evaluation of global simulations of aerosol par-  
 1135 ticle and cloud condensation nuclei number, with implications for cloud  
 1136 droplet formation. *Atmospheric Chemistry and Physics*, *19*, 8591–8617. doi:  
 1137 10.5194/acp-19-8591-2019
- 1138 Flato, G., Marotzke, J., Abiodun, B., Braconnot, P., Chou, S. C., Collins, W., ...  
 1139 Rummukainen, M. (2013). Climate change 2013: The physical science basis.  
 1140 contribution of working group I to the fifth assessment report of the inter-  
 1141 governmental panel on climate change [stocker, t.f., d. Qin, g.-k. Plattner, m.  
 1142 Tignor, s.k. Allen, j. Boschung, a. Nauels, y. Xia, v. Bex and p.m. Midgley (eds.)].  
 1143 In (pp. 741–882). Cambridge University Press, Cambridge, UK and New York,  
 1144 NY, USA. doi: 10.1017/CBO9781107415324.020
- 1145 Fossum, K. N., Ovadnevaite, J., Ceburnis, D., Dall’Osto, M., Marullo, S., Bellacicco,  
 1146 M., ... O’Dowd, C. (2018). Summertime Primary and Secondary Contribu-  
 1147 tions to Southern Ocean Cloud Condensation Nuclei. *Sci Rep*, *8*, 13844. doi:  
 1148 10.1038/s41598-018-32047-4
- 1149 Fossum, K. N., Ovadnevaite, J., Ceburnis, D., Preißler, J., Snider, J. R., Huang,  
 1150 R.-J., ... O’Dowd, C. (2020). Sea-spray regulates sulfate cloud droplet ac-  
 1151 tivation over oceans. *npj Climate and Atmospheric Science*, *3*, 1–6. doi:  
 1152 10.1038/s41612-020-0116-2
- 1153 Frey, M. M., Norris, S. J., Brooks, I. M., Anderson, P. S., Nishimura, K., Yang, X.,  
 1154 ... Wolff, E. W. (2020). First direct observation of sea salt aerosol production  
 1155 from blowing snow above sea ice. *Atmospheric Chemistry and Physics*, *20*,  
 1156 2549–2578. doi: 10.5194/acp-20-2549-2020
- 1157 Gliß, J., Mortier, A., Schulz, M., Andrews, E., Balkanski, Y., Bauer, S. E., ...  
 1158 Tsyro, S. G. (2021). AeroCom phase III multi-model evaluation of the aerosol  
 1159 life cycle and optical properties using ground- and space-based remote sensing  
 1160 as well as surface in situ observations. *Atmospheric Chemistry and Physics*,  
 1161 *21*, 87–128. doi: 10.5194/acp-21-87-2021

- 1162 Global Modeling and Assimilation Office. (2015). *MERRA2 taugM\_2d\_aer\_Nx:*  
 1163 *2d 1-Hourly Time-averaged Single-Level Assimilation Aerosol Diagnostics*  
 1164 *Monthly Mean, version 5.12.4 [Dataset].* (Goddard Space Flight Center Dis-  
 1165 tributed Active Archive Center (GSFC DAAC). Access date: 28 June 2022.  
 1166 doi: 10.5067/FH9A0MLJPC7N doi: 10.5067/FH9A0MLJPC7N
- 1167 Gong, S. L. (2003). A parameterization of sea-salt aerosol source function for sub-  
 1168 and super-micron particles. *Global Biogeochemical Cycles*, *17*. doi: 10.1029/  
 1169 2003GB002079
- 1170 Gryspeerd, E., Goren, T., Sourdeval, O., Quaas, J., Mülmenstädt, J., Dipu, S.,  
 1171 ... Christensen, M. (2019). Constraining the aerosol influence on cloud liq-  
 1172 uid water path. *Atmospheric Chemistry and Physics*, *19*, 5331–5347. doi:  
 1173 10.5194/acp-19-5331-2019
- 1174 Grythe, H., Ström, J., Krejci, R., Quinn, P., & Stohl, A. (2014). A review of sea-  
 1175 spray aerosol source functions using a large global set of sea salt aerosol con-  
 1176 centration measurements. *Atmospheric Chemistry and Physics*, *14*, 1277–1297.  
 1177 doi: 10.5194/acp-14-1277-2014
- 1178 Gutjahr, O., Putrasahan, D., Lohmann, K., Jungclaus, J. H., von Storch, J.-S.,  
 1179 Bruggemann, N., ... Stössel, A. (2019). Max Planck Institute Earth Sys-  
 1180 tem Model (MPI-ESM1.2) for the High-Resolution Model Intercomparison  
 1181 Project (HighResMIP). *Geoscientific Model Development*, *12*, 3241–3281. doi:  
 1182 10.5194/gmd-12-3241-2019
- 1183 Hajima, T., Watanabe, M., Yamamoto, A., Tatebe, H., Noguchi, M. A., Abe, M., ...  
 1184 Kawamiya, M. (2020). Development of the MIROC-ES2L Earth system model  
 1185 and the evaluation of biogeochemical processes and feedbacks. *Geoscientific*  
 1186 *Model Development*, *13*, 2197–2244. doi: 10.5194/gmd-13-2197-2020
- 1187 Hall, A. (2004). The Role of Surface Albedo Feedback in Climate. *Journal of Cli-*  
 1188 *mate*, *17*, 1550–1568. doi: 10.1175/1520-0442(2004)017<1550:TROSAF>2.0.CO;  
 1189 2
- 1190 Hara, K., Osada, K., Yabuki, M., Takashima, H., Theys, N., & Yamanouchi,  
 1191 T. (2018). Important contributions of sea-salt aerosols to atmospheric  
 1192 bromine cycle in the Antarctic coasts. *Sci Rep*, *8*, 13852. doi: 10.1038/  
 1193 s41598-018-32287-4
- 1194 Held, A., Brooks, I. M., Leck, C., & Tjernström, M. (2011). On the potential  
 1195 contribution of open lead particle emissions to the central Arctic aerosol  
 1196 concentration. *Atmospheric Chemistry and Physics*, *11*, 3093–3105. doi:  
 1197 10.5194/acp-11-3093-2011
- 1198 Hersbach, H., Bell, B., Berrisford, P., Biavati, G., Horányi, A., Muñoz Sabater, J.,  
 1199 ... Thépaut, J.-N. (2019). *ERA5 monthly averaged data on single levels from*  
 1200 *1959 to present [Dataset].* (Copernicus Climate Change Service (C3S) Climate  
 1201 Data Store (CDS). Access date: 20 July 2022. doi: 10.24381/cds.f17050d7 doi:  
 1202 10.24381/cds.f17050d7
- 1203 Heslin-Rees, D., Burgos, M., Hansson, H.-C., Krejci, R., Ström, J., Tunved, P., &  
 1204 Zieger, P. (2020). From a polar to a marine environment: has the chang-  
 1205 ing Arctic led to a shift in aerosol light scattering properties? *Atmospheric*  
 1206 *Chemistry and Physics*, *20*, 13671–13686. doi: 10.5194/acp-20-13671-2020
- 1207 Holtslag, A. a. M., Svensson, G., Baas, P., Basu, S., Beare, B., Beljaars, A. C. M.,  
 1208 ... Wiel, B. J. H. V. D. (2013). Stable Atmospheric Boundary Lay-  
 1209 ers and Diurnal Cycles: Challenges for Weather and Climate Models.  
 1210 *Bulletin of the American Meteorological Society*, *94*, 1691–1706. doi:  
 1211 10.1175/BAMS-D-11-00187.1
- 1212 Huang, J., & Jaeglé, L. (2017). Wintertime enhancements of sea salt aerosol in  
 1213 polar regions consistent with a sea ice source from blowing snow. *Atmospheric*  
 1214 *Chemistry and Physics*, *17*, 3699–3712. doi: 10.5194/acp-17-3699-2017
- 1215 Huang, Y., Ding, Q., Dong, X., Xi, B., & Baxter, I. (2021). Summertime low clouds  
 1216 mediate the impact of the large-scale circulation on Arctic sea ice. *Commun*

- 1217 *Earth Environ*, *2*, 1–10. doi: 10.1038/s43247-021-00114-w
- 1218 Inness, A., Ades, M., Agustí-Panareda, A., Barré, J., Benedictow, A., Blech-
- 1219 schmidt, A.-M., ... Suttie, M. (2019). The CAMS reanalysis of atmo-
- 1220 spheric composition. *Atmospheric Chemistry and Physics*, *19*, 3515–3556.
- 1221 doi: 10.5194/acp-19-3515-2019
- 1222 Ioannidis, E., Law, K. S., Raut, J.-C., Marelle, L., Onishi, T., Kirpes, R. M., ...
- 1223 Pratt, K. A. (2022). *Modelling wintertime Arctic Haze and sea-spray aerosols*
- 1224 (Tech. Rep.). Aerosols/Atmospheric Modelling/Troposphere/Chemistry (chem-
- 1225 ical composition and reactions). doi: 10.5194/egusphere-2022-310
- 1226 Jaeglé, L., Quinn, P. K., Bates, T. S., Alexander, B., & Lin, J.-T. (2011). Global
- 1227 distribution of sea salt aerosols: new constraints from in situ and remote sens-
- 1228 ing observations. *Atmospheric Chemistry and Physics*, *11*, 3137–3157. doi:
- 1229 10.5194/acp-11-3137-2011
- 1230 Kinne, S. (2019). The MACv2 aerosol climatology. *Tellus B: Chemical and Physical*
- 1231 *Meteorology*, *71*, 1–21. doi: 10.1080/16000889.2019.1623639
- 1232 Kirpes, R. M., Bonanno, D., May, N. W., Fraund, M., Barget, A. J., Moffet, R. C.,
- 1233 ... Pratt, K. A. (2019). Wintertime Arctic Sea Spray Aerosol Composition
- 1234 Controlled by Sea Ice Lead Microbiology. *ACS Cent. Sci.*, *5*, 1760–1767. doi:
- 1235 10.1021/acscentsci.9b00541
- 1236 Korhonen, H., Carslaw, K. S., Forster, P. M., Mikkonen, S., Gordon, N. D., &
- 1237 Kokkola, H. (2010). Aerosol climate feedback due to decadal increases in
- 1238 Southern Hemisphere wind speeds. *Geophysical Research Letters*, *37*. doi:
- 1239 10.1029/2009GL041320
- 1240 Kramer, S. J., Alvarez, C., Barkley, A. E., Colarco, P. R., Custals, L., Delgado,
- 1241 R., ... Zuidema, P. (2020). Apparent dust size discrepancy in aerosol reanal-
- 1242 ysis in north African dust after long-range transport. *Atmospheric Chemistry*
- 1243 *and Physics*, *20*, 10047–10062. doi: 10.5194/acp-20-10047-2020
- 1244 Lachlan-Cope, T. (2010). Antarctic clouds. *Polar Research*, *29*, 150–158. doi: 10
- 1245 .3402/polar.v29i2.6065
- 1246 Lapere, R. (2023a, January). *The representation of sea salt aerosols and their role in*
- 1247 *polar climate within CMIP6 [Dataset/Software]*. Zenodo. doi: 10.5281/zenodo
- 1248 .7590005
- 1249 Lapere, R. (2023b, January). *Sea salt aerosol AOD at 550nm derived from MODIS*
- 1250 *[Dataset]*. Zenodo. doi: 10.5281/zenodo.7584063
- 1251 Legrand, M., Yang, X., Preunkert, S., & Theys, N. (2016). Year-round records of sea
- 1252 salt, gaseous, and particulate inorganic bromine in the atmospheric boundary
- 1253 layer at coastal (Dumont d’Urville) and central (Concordia) East Antarctic
- 1254 sites. *Journal of Geophysical Research: Atmospheres*, *121*, 997–1023. doi:
- 1255 10.1002/2015JD024066
- 1256 Levine, J. G., Yang, X., Jones, A. E., & Wolff, E. W. (2014). Sea salt as an ice core
- 1257 proxy for past sea ice extent: A process-based model study. *Journal of Geo-*
- 1258 *physical Research: Atmospheres*, *119*, 5737–5756. doi: 10.1002/2013JD020925
- 1259 Li, S.-M., & Barrie, L. A. (1993). Biogenic sulfur aerosol in the Arctic troposphere:
- 1260 1. Contributions to total sulfate. *Journal of Geophysical Research: Atmo-*
- 1261 *spheres*, *98*, 20613–20622. doi: 10.1029/93JD02234
- 1262 Liu, S., Liu, C.-C., Froyd, K. D., Schill, G. P., Murphy, D. M., Bui, T. P., ... Gao,
- 1263 R.-S. (2021). Sea spray aerosol concentration modulated by sea surface tem-
- 1264 perature. *Proceedings of the National Academy of Sciences*, *118*, e2020583118.
- 1265 doi: 10.1073/pnas.2020583118
- 1266 Mahowald, N. M., Lamarque, J.-F., Tie, X. X., & Wolff, E. (2006). Sea-salt aerosol
- 1267 response to climate change: Last Glacial Maximum, preindustrial, and doubled
- 1268 carbon dioxide climates. *Journal of Geophysical Research: Atmospheres*, *111*.
- 1269 doi: 10.1029/2005JD006459
- 1270 Manabe, S., & Wetherald, R. T. (1975). The Effects of Doubling the CO<sub>2</sub> Concen-
- 1271 tration on the climate of a General Circulation Model. *Journal of the Atmo-*



- 1272 *spheric Sciences*, 32, 3–15. doi: 10.1175/1520-0469(1975)032<0003:TEODTC>2  
1273 .0.CO;2
- 1274 Mann, H. (1945). Nonparametric tests against trend. *Econometrica: Journal of the*  
1275 *Econometric Society*, 245–259. doi: 10.2307/1907187
- 1276 Marelle, L., Thomas, J. L., Ahmed, S., Tuite, K., Stutz, J., Dommergue, A., ...  
1277 Baladima, F. (2021). Implementation and Impacts of Surface and Blow-  
1278 ing Snow Sources of Arctic Bromine Activation Within WRF-Chem 4.1.1.  
1279 *Journal of Advances in Modeling Earth Systems*, 13, e2020MS002391. doi:  
1280 10.1029/2020MS002391
- 1281 McCrystall, M. R., Stroeve, J., Serreze, M., Forbes, B. C., & Screen, J. A. (2021).  
1282 New climate models reveal faster and larger increases in Arctic precipita-  
1283 tion than previously projected. *Nature Communications*, 12, 6765. doi:  
1284 10.1038/s41467-021-27031-y
- 1285 McCurry, P. (2000). A review of atmospheric aerosol measurements. *Atmos. Envi-*  
1286 *ron.*, 34, 1959–1999. doi: 10.1016/s1352-2310(99)00455-0
- 1287 Mei, L., Xue, Y., de Leeuw, G., von Hoyningen-Huene, W., Kokhanovsky, A. A.,  
1288 Istomina, L., ... Burrows, J. P. (2013). Aerosol optical depth retrieval in the  
1289 Arctic region using MODIS data over snow. *Remote Sensing of Environment*,  
1290 128, 234–245. doi: 10.1016/j.rse.2012.10.009
- 1291 Meinander, O., Dagsson-Waldhauserova, P., Amosov, P., Aseyeva, E., Atkins, C.,  
1292 Baklanov, A., ... Vukovic Vimic, A. (2022). Newly identified climatically and  
1293 environmentally significant high-latitude dust sources. *Atmospheric Chemistry*  
1294 *and Physics*, 22, 11889–11930. doi: 10.5194/acp-22-11889-2022
- 1295 Meredith, M., Sommerkorn, M., Cassotta, S., Derksen, C., Ekaykin, A., Hollowed,  
1296 A., ... Schuur, E. (2019). IPCC Special Report on the Ocean and Cryosphere  
1297 in a Changing Climate [H.-O. Pörtner, D. C. Roberts, V. Masson-Delmotte,  
1298 P. Zhai, M. Tignor, E. Poloczanska, K. Mintenbeck, A. Alegria, M. Nico-  
1299 lai, A. Okem, J. Petzold, B. Rama, N. M. Weyer (eds.)]. In (p. 203-320).  
1300 Cambridge University Press, Cambridge, UK and New York, NY, USA. doi:  
1301 10.1017/9781009157964.005
- 1302 Miller, R. L., Schmidt, G. A., Nazarenko, L. S., Bauer, S. E., Kelley, M., Ruedy, R.,  
1303 ... Yao, M.-S. (2021). CMIP6 Historical Simulations (1850–2014) With GISS-  
1304 E2.1. *Journal of Advances in Modeling Earth Systems*, 13, e2019MS002034.  
1305 doi: 10.1029/2019MS002034
- 1306 Monahan, E. C., Spiel, D. E., & Davidson, K. L. (1986). A Model of Marine  
1307 Aerosol Generation Via Whitecaps and Wave Disruption. In E. C. Mon-  
1308 ahan & G. M. Niocaill (Eds.), *Oceanic Whitecaps: And Their Role in*  
1309 *Air-Sea Exchange Processes* (pp. 167–174). Springer Netherlands. doi:  
1310 10.1007/978-94-009-4668-2\_16
- 1311 Mortier, A., Gliß, J., Schulz, M., Aas, W., Andrews, E., Bian, H., ... Tilmes, S.  
1312 (2020). Evaluation of climate model aerosol trends with ground-based observa-  
1313 tions over the last 2 decades – an AeroCom and CMIP6 analysis. *Atmospheric*  
1314 *Chemistry and Physics*, 20, 13355–13378. doi: 10.5194/acp-20-13355-2020
- 1315 Murphy, D. M., Froyd, K. D., Bian, H., Brock, C. A., Dibb, J. E., DiGangi, J. P.,  
1316 ... Yu, P. (2019). The distribution of sea-salt aerosol in the global tropo-  
1317 sphere. *Atmospheric Chemistry and Physics*, 19, 4093–4104. doi:  
1318 10.5194/acp-19-4093-2019
- 1319 Myhre, G., Shindell, D., Bréon, F.-M., Collins, W., Fuglestedt, J., Huang, J., ...  
1320 Zhang, H. (2013). Climate Change 2013: The Physical Science Basis. Contri-  
1321 bution of Working Group I to the Fifth Assessment Report of the Intergovern-  
1322 mental Panel on Climate Change [Stocker, T.F., D. Qin, G.-K. Plattner, M.  
1323 Tignor, S.K. Allen, J. Boschung, A. Nauels, Y. Xia, V. Bex and P.M. Midgley  
1324 (eds.)]. In (chap. Anthropogenic and Natural Radiative Forcing). Cambridge  
1325 University Press, Cambridge, UK and New York, NY, USA.
- 1326 Mårtensson, E. M., Nilsson, E. D., de Leeuw, G., Cohen, L. H., & Hansson, H.-C.

- 1327 (2003). Laboratory simulations and parameterization of the primary marine  
 1328 aerosol production. *Journal of Geophysical Research: Atmospheres*, *108*. doi:  
 1329 10.1029/2002JD002263
- 1330 Nilsson, E. D., Rannik, U., Swietlicki, E., Leck, C., Aalto, P. P., Zhou, J., & Nor-  
 1331 man, M. (2001). Turbulent aerosol fluxes over the Arctic Ocean: 2. Wind-  
 1332 driven sources from the sea. *Journal of Geophysical Research: Atmospheres*,  
 1333 *106*, 32139–32154. doi: 10.1029/2000JD900747
- 1334 Norwegian Institute for Air Research. (2022). *Ebas*. Retrieved from <https://ebas>  
 1335 [.nilu.no/](https://ebas.nilu.no/)
- 1336 Notz, D., & SIMIP Community. (2020). Arctic Sea Ice in CMIP6. *Geophysical Re-*  
 1337 *search Letters*, *47*, e2019GL086749. doi: 10.1029/2019GL086749
- 1338 O'Neill, B. C., Tebaldi, C., van Vuuren, D. P., Eyring, V., Friedlingstein, P., Hurtt,  
 1339 G., ... Sanderson, B. M. (2016). The Scenario Model Intercomparison Project  
 1340 (ScenarioMIP) for CMIP6. *Geoscientific Model Development*, *9*, 3461–3482.  
 1341 doi: 10.5194/gmd-9-3461-2016
- 1342 Palerme, C., Genthon, C., Claud, C., Kay, J. E., Wood, N. B., & L'Ecuyer, T.  
 1343 (2017). Evaluation of current and projected Antarctic precipitation in CMIP5  
 1344 models. *Climate Dynamics*, *48*, 225–239. doi: 10.1007/s00382-016-3071-1
- 1345 Platnick, S. (2015). *MODIS Atmosphere L3 Monthly Product [Dataset]*. (NASA  
 1346 MODIS Adaptive Processing System, Goddard Space Flight Center, USA.  
 1347 Access date: 20 July 2022, doi: 10.5067/MODIS/MOD08\_M3.006) doi:  
 1348 10.5067/MODIS/MOD08\\_M3.006
- 1349 Prank, M., Tonttila, J., Ahola, J., Kokkola, H., Kühn, T., Romakkaniemi, S., &  
 1350 Raatikainen, T. (2022). Impacts of marine organic emissions on low-level  
 1351 stratiform clouds – a large eddy simulator study. *Atmospheric Chemistry and*  
 1352 *Physics*, *22*, 10971–10992. doi: 10.5194/acp-22-10971-2022
- 1353 Qi, L., Li, Q., Li, Y., & He, C. (2017). Factors controlling black carbon distribu-  
 1354 tion in the Arctic. *Atmospheric Chemistry and Physics*, *17*, 1037–1059. doi: 10  
 1355 .5194/acp-17-1037-2017
- 1356 Quinn, P. K., Coffman, D. J., Johnson, J. E., Upchurch, L. M., & Bates, T. S.  
 1357 (2017). Small fraction of marine cloud condensation nuclei made up of sea  
 1358 spray aerosol. *Nature Geosci*, *10*, 674–679. doi: 10.1038/ngeo3003
- 1359 Quinn, P. K., Miller, T. L., Bates, T. S., Ogren, J. A., Andrews, E., & Shaw, G. E.  
 1360 (2002). A 3-year record of simultaneously measured aerosol chemical and  
 1361 optical properties at Barrow, Alaska. *Journal of Geophysical Research: Atmo-*  
 1362 *spheres*, *107*, 8–15. doi: 10.1029/2001JD001248
- 1363 Rantanen, M., Karpechko, A. Y., Lipponen, A., Nordling, K., Hyvärinen, O., Ru-  
 1364 osteenoja, K., ... Laaksonen, A. (2022). The Arctic has warmed nearly four  
 1365 times faster than the globe since 1979. *Commun Earth Environ*, *3*, 1–10. doi:  
 1366 10.1038/s43247-022-00498-3
- 1367 Regayre, L. A., Schmale, J., Johnson, J. S., Tatzelt, C., Baccarini, A., Henning, S.,  
 1368 ... Carslaw, K. S. (2020). The value of remote marine aerosol measurements  
 1369 for constraining radiative forcing uncertainty. *Atmospheric Chemistry and*  
 1370 *Physics*, *20*, 10063–10072. doi: 10.5194/acp-20-10063-2020
- 1371 Rhodes, R. H., Yang, X., & Wolff, E. W. (2018). Sea Ice Versus Storms: What  
 1372 Controls Sea Salt in Arctic Ice Cores? *Geophysical Research Letters*, *45*, 5572–  
 1373 5580. doi: 10.1029/2018GL077403
- 1374 Roach, L. A., Dörr, J., Holmes, C. R., Massonnet, F., Blockley, E. W., Notz, D., ...  
 1375 Bitz, C. M. (2020). Antarctic Sea Ice Area in CMIP6. *Geophysical Research*  
 1376 *Letters*, *47*, e2019GL086729. doi: 10.1029/2019GL086729
- 1377 Roussel, M.-L., Lemonnier, F., Genthon, C., & Krinner, G. (2020). Brief  
 1378 communication: Evaluating Antarctic precipitation in ERA5 and CMIP6  
 1379 against CloudSat observations. *The Cryosphere*, *14*, 2715–2727. doi:  
 1380 10.5194/tc-14-2715-2020
- 1381 Salter, M. E., Zieger, P., Acosta Navarro, J. C., Grythe, H., Kirkevåg, A., Rosati,

- 1382 B., ... Nilsson, E. D. (2015). An empirically derived inorganic sea spray  
 1383 source function incorporating sea surface temperature. *Atmospheric Chemistry  
 1384 and Physics*, *15*, 11047–11066. doi: 10.5194/acp-15-11047-2015
- 1385 Samset, B. H. (2022). Aerosol absorption has an underappreciated role in historical  
 1386 precipitation change. *Communications Earth & Environment*, *3*, 1–8. doi: 10  
 1387 .1038/s43247-022-00576-6
- 1388 Sand, M., Samset, B. H., Balkanski, Y., Bauer, S., Bellouin, N., Berntsen, T. K.,  
 1389 ... Zhang, H. (2017). Aerosols at the poles: an AeroCom Phase II multi-  
 1390 model evaluation. *Atmospheric Chemistry and Physics*, *17*, 12197–12218. doi:  
 1391 10.5194/acp-17-12197-2017
- 1392 Sand, M., Samset, B. H., Myhre, G., Gliß, J., Bauer, S. E., Bian, H., ... Watson-  
 1393 Parris, D. (2021). Aerosol absorption in global models from AeroCom  
 1394 phase III. *Atmospheric Chemistry and Physics*, *21*, 15929–15947. doi:  
 1395 10.5194/acp-21-15929-2021
- 1396 Satheesh, S. K., & Lubin, D. (2003). Short wave versus long wave radiative forcing  
 1397 by Indian Ocean aerosols: Role of sea-surface winds. *Geophysical Research Let-  
 1398 ters*, *30*. doi: 10.1029/2003GL017499
- 1399 Sayer, A. M., Hsu, N. C., Bettenhausen C., & Jeong, M.-J. (2013). Validation and  
 1400 uncertainty estimates for MODIS Collection 6 “Deep Blue” aerosol data. *J.  
 1401 Geophys. Res. Atmos.*, *118*, 7864–7872. doi: 10.1002/jgrd.50600
- 1402 Schmale, J., Zieger, P., & Ekman, A. M. L. (2021). Aerosols in current and future  
 1403 Arctic climate. *Nat. Clim. Chang.*, *11*, 95–105. doi: 10.1038/s41558-020-00969  
 1404 -5
- 1405 Schulzweida, U., Kornbluh, L., & Quast, R. (2012). *Climate Data Operators  
 1406 User’s Guide - Version 1.5.9* (Tech. Rep.). MPI for Meteorology, Brockmann  
 1407 Consult.
- 1408 Seinfeld, J. H., & Pandis, S. N. (2016). *Atmospheric Chemistry and Physics: From  
 1409 Air Pollution to Climate Change, 3rd Edition*. Wiley.
- 1410 Seland, O., Bentsen, M., Olivie, D., Toniazzo, T., Gjermundsen, A., Graff, L. S.,  
 1411 ... Schulz, M. (2020). Overview of the Norwegian Earth System Model  
 1412 (NorESM2) and key climate response of CMIP6 DECK, historical, and sce-  
 1413 nario simulations. *Geoscientific Model Development*, *13*, 6165–6200. doi:  
 1414 10.5194/gmd-13-6165-2020
- 1415 Sellar, A. A., Walton, J., Jones, C. G., Wood, R., Abraham, N. L., Andrejczuk, M.,  
 1416 ... Griffiths, P. T. (2020). Implementation of U.K. Earth System Models for  
 1417 CMIP6. *Journal of Advances in Modeling Earth Systems*, *12*, e2019MS001946.  
 1418 doi: 10.1029/2019MS001946
- 1419 Smith, D. M., Screen, J. A., Deser, C., Cohen, J., Fyfe, J. C., García-Serrano, J., ...  
 1420 Zhang, X. (2019). The Polar Amplification Model Intercomparison Project  
 1421 (PAMIP) contribution to CMIP6: investigating the causes and consequences  
 1422 of polar amplification. *Geoscientific Model Development*, *12*, 1139–1164. doi:  
 1423 10.5194/gmd-12-1139-2019
- 1424 Smith, M. H., & Harrison, N. M. (1998). The sea spray generation function. *Journal  
 1425 of Aerosol Science*, *29*, S189–S190. doi: 10.1016/S0021-8502(98)00280-8
- 1426 Sogacheva, L., Popp, T., Sayer, A. M., Dubovik, O., Garay, M. J., Heckel, A., ...  
 1427 Arola, A. (2020). Merging regional and global aerosol optical depth records  
 1428 from major available satellite products. *Atmospheric Chemistry and Physics*,  
 1429 *20*, 2031–2056. doi: 10.5194/acp-20-2031-2020
- 1430 Struthers, H., Ekman, A. M. L., Glantz, P., Iversen, T., Kirkevåg, A., Seland, O.,  
 1431 ... Nilsson, E. D. (2013). Climate-induced changes in sea salt aerosol number  
 1432 emissions: 1870 to 2100. *Journal of Geophysical Research: Atmospheres*, *118*,  
 1433 670–682. doi: 10.1002/jgrd.50129
- 1434 Struthers, H., Ekman, A. M. L., Glantz, P., Iversen, T., Kirkevåg, A., Mårtensson,  
 1435 E. M., ... Nilsson, E. D. (2011). The effect of sea ice loss on sea salt aerosol  
 1436 concentrations and the radiative balance in the Arctic. *Atmospheric Chemistry*

- 1437 *and Physics*, 11, 3459–3477. doi: 10.5194/acp-11-3459-2011
- 1438 Stuecker, M. F., Bitz, C. M., Armour, K. C., Proistosescu, C., Kang, S. M.,  
 1439 Xie, S.-P., ... Jin, F.-F. (2018). Polar amplification dominated by lo-  
 1440 cal forcing and feedbacks. *Nature Climate Change*, 8, 1076–1081. doi:  
 1441 10.1038/s41558-018-0339-y
- 1442 Séférian, R., Nabat, P., Michou, M., Saint-Martin, D., Voldoire, A., Colin, J., ...  
 1443 Madec, G. (2019). Evaluation of CNRM Earth System Model, CNRM-ESM2-  
 1444 1: Role of Earth System Processes in Present-Day and Future Climate. *J. Adv.*  
 1445 *Model. Earth Syst.*, 11, 4182–4227. doi: 10.1029/2019MS001791
- 1446 Takemura, T., Nakajima, T., Dubovik, O., Holben, B. N., & Kinne, S. (2002).  
 1447 Single-Scattering Albedo and Radiative Forcing of Various Aerosol Species  
 1448 with a Global Three-Dimensional Model. *Journal of Climate*, 15, 333–352.  
 1449 doi: 10.1175/1520-0442(2002)015(0333:SSAARF)2.0.CO;2
- 1450 Tang, M. S. Y., Chenoli, S. N., Samah, A. A., & Hai, O. S. (2018). An as-  
 1451 sessment of historical Antarctic precipitation and temperature trend us-  
 1452 ing CMIP5 models and reanalysis datasets. *Polar Science*, 15, 1–12. doi:  
 1453 10.1016/j.polar.2018.01.001
- 1454 Tewari, K., Mishra, S. K., Salunke, P., & Dewan, A. (2022). Future projections of  
 1455 temperature and precipitation for Antarctica. *Environmental Research Letters*,  
 1456 17, 014029. doi: 10.1088/1748-9326/ac43e2
- 1457 Thornhill, G., Collins, W., Olivie, D., Skeie, R. B., Archibald, A., Bauer, S., ...  
 1458 Weber, J. (2021). Climate-driven chemistry and aerosol feedbacks in CMIP6  
 1459 Earth system models. *Atmospheric Chemistry and Physics*, 21, 1105–1126.  
 1460 doi: 10.5194/acp-21-1105-2021
- 1461 Tunved, P., Ström, J., & Krejci, R. (2013). Arctic aerosol life cycle: linking aerosol  
 1462 size distributions observed between 2000 and 2010 with air mass transport  
 1463 and precipitation at Zeppelin station, Ny-Ålesund, Svalbard. *Atmospheric*  
 1464 *Chemistry and Physics*, 13, 3643–3660. doi: 10.5194/acp-13-3643-2013
- 1465 Turner, J., Comiso, J. C., Marshall, G. J., Lachlan-Cope, T. A., Bracegirdle, T.,  
 1466 Maksym, T., ... Orr, A. (2009). Non-annular atmospheric circulation  
 1467 change induced by stratospheric ozone depletion and its role in the recent  
 1468 increase of Antarctic sea ice extent. *Geophysical Research Letters*, 36. doi:  
 1469 10.1029/2009GL037524
- 1470 Vavrus, S. J., & Alkama, R. (2022). Future trends of arctic surface wind speeds and  
 1471 their relationship with sea ice in CMIP5 climate model simulations. *Clim Dyn*,  
 1472 59, 1833–1848. doi: 10.1007/s00382-021-06071-6
- 1473 Wilson, T. W., Ladino, L. A., Alpert, P. A., Breckels, M. N., Brooks, I. M., Browse,  
 1474 J., ... Murray, B. J. (2015). A marine biogenic source of atmospheric ice-  
 1475 nucleating particles. *Nature*, 525, 234–238. doi: 10.1038/nature14986
- 1476 Wu, T., Zhang, F., Zhang, J., Jie, W., Zhang, Y., Wu, F., ... Hu, A. (2020). Beijing  
 1477 Climate Center Earth System Model version 1 (BCC-ESM1): model descrip-  
 1478 tion and evaluation of aerosol simulations. *Geoscientific Model Development*,  
 1479 13, 977–1005. doi: 10.5194/gmd-13-977-2020
- 1480 Xian, P., Zhang, J., O’Neill, N. T., Toth, T. D., Sorenson, B., Colarco, P. R., ...  
 1481 Ranjbar, K. (2022). Arctic spring and summertime aerosol optical depth  
 1482 baseline from long-term observations and model reanalyses – Part 1: Clima-  
 1483 tology and trend. *Atmospheric Chemistry and Physics*, 22, 9915–9947. doi:  
 1484 10.5194/acp-22-9915-2022
- 1485 Xu, W., Ovadnevaite, J., Fossom, K. N., Lin, C., Huang, R.-J., Ceburnis, D., &  
 1486 O’Dowd, C. (2022). Sea spray as an obscured source for marine cloud nuclei.  
 1487 *Nat. Geosci.*, 15, 282–286. doi: 10.1038/s41561-022-00917-2
- 1488 Yang, X., Frey, M. M., Rhodes, R. H., Norris, S. J., Brooks, I. M., Anderson, P. S.,  
 1489 ... Wolff, E. W. (2019). Sea salt aerosol production via sublimating wind-  
 1490 blown saline snow particles over sea ice: parameterizations and relevant micro-  
 1491 physical mechanisms. *Atmospheric Chemistry and Physics*, 19, 8407–8424. doi:

- 1492 10.5194/acp-19-8407-2019  
1493 Yang, X., Pyle, J. A., & Cox, R. A. (2008). Sea salt aerosol production and bromine  
1494 release: Role of snow on sea ice. *Geophysical Research Letters*, *35*. doi: 10  
1495 .1029/2008GL034536  
1496 Yukimoto, S., Kawai, H., Koshiro, T., Oshima, N., Yoshida, K., Urakawa, S., ...  
1497 Ishii, M. (2019). The Meteorological Research Institute Earth System Model  
1498 Version 2.0, MRI-ESM2.0: Description and Basic Evaluation of the Physical  
1499 Component. *Journal of the Meteorological Society of Japan*, *97*, 931–965. doi:  
1500 10.2151/jmsj.2019-051  
1501 Zhu, L., Jacob, D. J., Eastham, S. D., Sulprizio, M. P., Wang, X., Sherwen, T., ...  
1502 Percival, C. J. (2019). Effect of sea salt aerosol on tropospheric bromine  
1503 chemistry. *Atmospheric Chemistry and Physics*, *19*, 6497–6507. doi:  
1504 10.5194/acp-19-6497-2019  
1505 Zieger, P., Väisänen, O., Corbin, J. C., Partridge, D. G., Bastelberger, S., Mousavi-  
1506 Fard, M., ... Salter, M. E. (2017). Revising the hygroscopicity of inorganic sea  
1507 salt particles. *Nature Communications*, *8*, 15883. doi: 10.1038/ncomms15883  
1508 Zinke, J., Nilsson, E. D., Zieger, P., & Salter, M. E. (2022). The Effect of Seawa-  
1509 ter Salinity and Seawater Temperature on Sea Salt Aerosol Production. *Jour-  
1510 nal of Geophysical Research: Atmospheres*, *127*, e2021JD036005. doi: 10.1029/  
1511 2021JD036005  
1512 Zábori, J., Krejci, R., Ekman, A. M. L., Mårtensson, E. M., Ström, J., de Leeuw,  
1513 G., & Nilsson, E. D. (2012). Wintertime Arctic Ocean sea water proper-  
1514 ties and primary marine aerosol concentrations. *Atmospheric Chemistry and  
1515 Physics*, *12*, 10405–10421. doi: 10.5194/acp-12-10405-2012